Predicting the influence of geometric imperfections on the mechanical response of 2D and 3D periodic trusses

R.N. Glaesener[a], S. Kumar[c], C. Lestringant[d], T. Butruille[b], C.M. Portela[b], D.M. Kochmann[a,*]

[a]*Mechanics & Materials Lab, Department of Mechanical and Process Engineering, ETH Zürich, 8092 Zürich, Switzerland*
[b]*Department of Mechanical Engineering, Massachusetts Institute of Technology, 77 Massachusetts Avenue, Cambridge, MA 02139, USA*
[c]*Delft University of Technology, Mekelweg 2, 2628CD, The Netherlands*
[d]*Institut ∂'Alembert, CNRS, Sorbonne Université, 75005 Paris, France*

Abstract

Although architected materials based on truss networks have been shown to possess advantageous or extreme mechanical properties, those can be highly affected by tolerances and uncertainties in the manufacturing process, which are usually neglected during the design phase. Deterministic computational tools typically design structures with the assumption of perfect, *defect-free* architectures, while experiments have confirmed the inevitable presence of imperfections and their possibly detrimental impact on the effective properties. Information about the nature and expected magnitude of geometric defects that emerge from the additive manufacturing processes would allow for new designs that aim to mitigate (or at least account for) the effects of defects and to reduce the uncertainty in the effective properties. To this end, we here investigate the effects of four most commonly found types of geometric imperfections in trusses, applied to eleven representative truss topologies in two and three dimensions. Through our study, we *(i)* quantify the impact of imperfections on the effective stiffness through computational homogenization, *(ii)* examine the sensitivity of the various truss topologies with respect to those imperfections, *(iii)* demonstrate the applicability of the model through experiments on 3D-printed trusses, and *(iv)* present a machine learning framework to predict the presence of defects in a given truss architecture based merely on its mechanical response.

Keywords: Truss, Imperfection, Elasticity, Metamaterial, Finite element method, Machine learning

1. Introduction

Although additive manufacturing (AM) has enabled the fabrication of micro-architected materials with complex geometries and topologies [1], the probability of producing unwanted structural imperfections grows as feature sizes decrease, especially down to the resolution limits of the printing process [2]. This may result in significant differences between the as-designed, nominal properties of, e.g., truss-based architected materials as obtained from theoretical predictions and the experimentally observed properties of trusses [3–5]. Models based on the nominal, as-designed

*Phone +41-44-632-32-76
Email address: dmk@ethz.ch (D.M. Kochmann)

architecture of trusses tend to overestimate their fabricated counterparts' stiffness, strength, and toughness, and discrepancies can typically be attributed to the emergence of imperfections and defects during the manufacturing process [6, 7]. This not only implies inaccurate property predictions; it also puts limitations on the theoretical/computational search for optimal metamaterial architectures, which usually assume an ideal, defect-free fabrication process with as-designed truss geometry and base material properties. Optimization with imperfections has been addressed only in recent years [8] and has remained a challenge (especially if the exact details of the imperfections is not known a priori). Imperfections can both be advantageous and disadvantageous. While buckling loads, e.g., can be strongly reduced by symmetry-breaking imperfections, imperfections in the form of small perturbations have been exploited to promote pre-defined buckling patterns in loaded structures [9].

In many studies, the experimentally predicted strength, stiffness, and failure modes of trusses have shown discrepancies when compared to their as-designed counterparts [10–13], which has been attributed to different defect types introduced in the fabrication process at the architectural and base material levels [14]. The high sensitivity of architected materials to fabrication defects stems, among others, from the oftentimes used periodic architectural design (rich in symmetries to be broken by imperfections) as well as from the high stiffness-to-density ratio (which leads to architectures composed of slender members that guide non-redundant load paths through the lattice) [8]. Small perturbations in the load-optimized topology result in a behavior different from the computationally designed one, causing a potentially significant deterioration of the effective response.

These uncertainties in the mechanical response require careful consideration when designing architected materials not only for industrial applications. To overcome this problem, which is one of the culprits preventing metamaterials from their entrance into many real-life applications, fabrication processes must become more precise or we must learn to understand the architected materials' sensitivity to imperfections and take it into account during the design process [15, 16].

The most common imperfections observed in trusses can be classified into two categories. First, visualized in Figure 1, *geometric defects* such as (a) variations of the beam *cross-section*'s shapes and beam surface roughness, (b) beam waviness (observed especially in small-scale 3D-printing based on lithographic techniques), (c) perturbations of the locations of nodes, and (d) the presence of broken beams[1]. The second category of defects concerns process-induced *base material heterogeneity*, such as non-uniform mechanical properties due to inclusions or variations in composition, cross-linking, and porosity.

A widely used categorization of lattices is based on their number of nodal connectivities, Z, which defines stretching- vs. bending-dominated trusses (also termed kinematically rigid vs. non-rigid, respectively). In *two dimensions* (2D), trusses with low nodal connectivity are most affected by the occurrence of broken beams [17, 18]. Moreover, studies discovered that the kagome lattice ($Z = 3$) switches its deformation mode from stretching- to

[1] Here and in the following, we refer to struts inside a truss as *beams*, irrespective of their primary deformation modes. In addition, we refer to *nodes* as the junctions between beams.

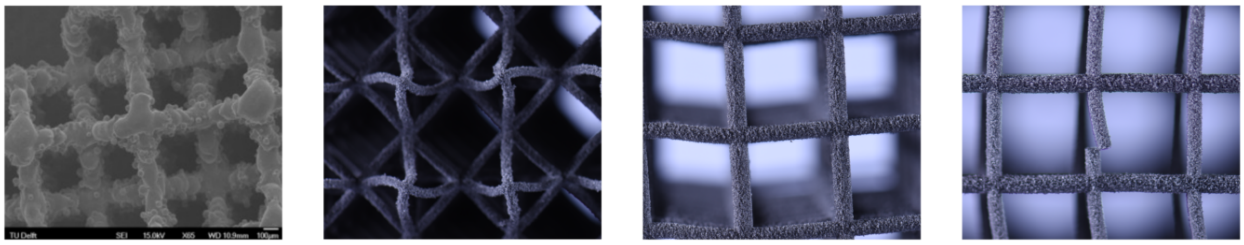

(a) diameter variation (b) wavy beams (c) node displacement (d) broken beams

Figure 1: Four types of imperfections are presented that commonly appear during the fabrication process. Subfigure (a) is reprinted by permission from Elsevier [6]. Figures (b) - (d) fabricated with selective laser sintering (SLS) on a Sintratec S1 printer.

bending-dominated in case of a large fraction of broken beams. The sensitivity of the effective stiffness with respect to missing beams was studied for the hexagonal lattice [19, 20] and non-periodic Voronoi topologies [21–23].

In *three dimensions* (3D), an extensive study of the truss sensitivity to defects was reported in [14], where the homogenized properties of imperfect 3D lattices were studied in both the linear elastic and nonlinear regimes. Their experiments revealed that manufacturing settings, such as the building direction and 3D-print scanning rate, result in a non-uniform deterioration of the mechanical properties. Moreover, they discovered that the octet unit cell is remarkably sensitive to geometric imperfections such as strut waviness and thickness variations, which also affects the failure mechanisms. Studies that focused on the impact of the size and distribution of voids in a truss topology on its homogenized elastic properties discovered that the void volume fraction dominates the degradation of the mechanical properties over the void size [24]. Others observed the same knock-down effect in stiffness due to strut waviness in 3D topologies as previously reported for 2D structures [25]. Similarly, studies reported the importance of diameter variations [6, 26] and missing beams [27, 28]. Few experimental studies on 3D metallic truss-based architected materials investigated the influence of fabrication-induced imperfections on different truss topologies [29, 30]. These are only a few examples from the broad literature available on additive manufacturing and imperfect trusses.

While the sensitivity to imperfections of truss metamaterials and other cellular structures has been extensively investigated in the past, most of the above studies focus on either 2D or 3D trusses, on a unique type of imperfection, or on a particular lattice topology. Statements and outcomes are specific to the types of imperfections and the truss topologies studied, while a general overview is missing. Most of the presented studies rely on experimental observations, only a few have taken on the challenge of introducing predictive models for imperfect trusses. Finding general statements about the influence of imperfections or even predictive models is challenging, as it strongly depends on the truss topology, the cross-sectional geometry, the constituent material, and the effective property of interest. Most numerical modeling techniques for trusses have hence relied on perfectly symmetric, periodic, and defect-free truss lattices [31–35], whose predictions have limited validity in the presence of defects. Those few models that have captured the mechanical response of imperfect trusses were limited to a small selection of topologies and imperfection

types [14, 17, 24]. Moreover, the distribution of imperfections in real-world trusses in stochastic (no two 3D-printed trusses are alike), so that a statistical approach is required, which increases the modeling complexity and cost.

To gain insight into the effect of imperfections on the effective properties of periodic trusses (exemplified by their anisotropic stiffness), we here investigate the effects of four most commonly found types of morphological defects in trusses, applied to 11 representative truss topologies in 2D and 3D. To this end, we introduce a statistical description of imperfections, which allows us to intentionally include defects into ideal trusses—both in experiments and in the model. The chosen statistical defect distributions are rationalized by experimental observations from Selective Laser Melting (SLM) additive manufacturing processes [14, 36].

Defects are introduced spatially randomly across a representative volume element (RVE), not considering any specific underlying causal mechanisms (such as print directions or material anisotropy). By intentionally incorporating the as-designed imperfections into 3D-printed periodic trusses, we experimentally assess its effective response. As a typical effective response that is easily computed, we determine the homogenized stiffness tensor (using affine boundary conditions for an upper bound, as the imperfect RVE is in general non-periodic). To compare with experiments and to validate the model, we further perform simulations of uniaxial (vertical) compression with fixed boundary conditions at the top and bottom.

Both approaches provide a rich set of data, which we subsequently use to train machine learning models that predict the imperfection probability distribution based on a given structure's effective mechanical response. Overall, while our forward model highlights the sensitivity of different truss topologies to imperfection types and magnitudes for a given distribution of defects, the inverse model predicts the defect distribution in a truss whose effective elastic moduli are known.

The remainder of this manuscript is structured as follows. We introduce the statistical description of imperfections in Section 2 and discuss their theoretical implementation. In Section 3 we present the homogenized stiffness properties and select the RVE size based on the necessary confidence interval to yield a sufficient statistical representation. Section 4 studies the mechanical sensitivity of 2D and 3D trusses to imperfections of different magnitudes. A validation of the proposed model with experiments is presented in Section 5. The machine learning model summarized in Section 6 finally allows us to invert the framework and to predict the type and probability distribution of imperfections in a truss on the basis of its effective elastic moduli. Section 7 concludes this study.

2. Statistical description of imperfections in slender trusses

We consider periodic networks of slender trusses, whose topology and geometry are encoded in the architecture on a single unit cell (UC). The unit cell contains n_n nodes, which are rigidly connected by n_b straight beams of constant cross-section. Specifically, we assume circular cross-sections of area $A = \frac{\pi D^2}{4}$, where D is the cross-sectional diameter, which is assumed constant along the length of each beam length. The area moment of inertia against bending is $I = \frac{\pi}{64} D^4$. The slenderness of a beam is characterized by the ratio $\lambda = \frac{D}{L}$ with L denoting the beam length. Here and

in the following, all (nominal) geometric parameters of the as-designed truss are denoted by capital letters, whereas those of the imperfect truss are described by lower-case letters. The base material is assumed to be homogeneous, isotropic, linear elastic so that, along with sufficient slenderness, beams adhere to Euler-Bernoulli beam theory.

Starting from the nominal (perfect) design of a truss architecture, we consider a statistical distribution of defects, which lead to the imperfect truss. Rather than characterizing defects experimentally (which would necessarily depend on a particular fabrication route), we focus on the four most frequently observed types of imperfections, which we apply to the perfect trusses to produce the imperfect trusses used in our simulations. The choice of the specific statistical distributions and the imperfection magnitudes can be adapted for particular processing routes with known defect distributions, which may, of course, affect the reported results. While the presented forward prediction techniques generally apply to arbitrary magnitudes of imperfections, the inverse design may be sensitive to the imperfection magnitude, and we here restrict our study to the imperfection types described below.

The four types of imperfections considered in the following are:

- **Node displacements:** many printed samples show errors in the positioning of the nodes [37]. We replicate this imperfection by perturbing every undeformed node location. Specifically, the node's center location is randomly displaced onto the surface of a sphere in 3D (or circle in 2D), which has radius r_{nds} and is centered at the nominal node position, as shown in Figure 2(a). The imperfect position of a node originally at (X, Y, Z) is hence

$$(x, y, z) = (X, Y, Z) + r_{\text{nds}} \left(\sqrt{1 - \cos^2\theta}\cos\phi,\ \sqrt{1 - \cos^2\theta}\sin\phi, \cos\theta \right), \tag{1}$$

  where the polar angles θ and ϕ are drawn from uniform distributions such that $\phi \in [0, 2\pi]$ and $\theta \in [0, \pi]$. (In 2D, the analogous description follows from fixing $\theta = \frac{\pi}{2}$.) As a realistic approximation of the displacement amplitude (here, radius r_{nds}), we assume a half-Gaussian distribution centered at $\mu = 0$ and having the standard deviation $\sigma = \xi_{\text{nds}} L$ (L being a characteristic beam length in the RVE). r_{nds} then follows from a Box-Muller transform [38]. Parameter $\xi_{\text{nds}} \in [0, 1]$ is used in the following to control the severity of the node displacements. In all of the following examples, we do not allow this imperfection to lie outside $\xi_{\text{nds}} \in [0, 0.3]$, which includes strong defects while avoiding the merging of adjacent nodes.

- **Missing beams:** a worst-case scenario, absent beams imply a missing nodal connection, which we implement by removing beams from the truss, as visualized in Figure 2(b). Missing beams appear during the printing process (or afterwards) when a previously intact beam breaks or is not printed properly. Parameter $\xi_{\text{mis}} \in [0, 1]$ denotes the ratio of the number of missing beams to the total number of beams in the RVE (where $\xi = 0$ implies all beams are intact, while $\xi = 1$ means no connectivity between nodes). We select the missing beam by a Bernoulli distribution with probability ξ_{mis}. In practice, rather than altering the finite element connectivity in the RVE, we reduce the Youngs's modulus of each missing beam to 10^{-10} its original value. (The impact of this approximation on the outcome was verified to be negligible.) In case of using beams that are refined into multiple beam elements (as required for the implementation of wavy beams), all elements of a given strut are

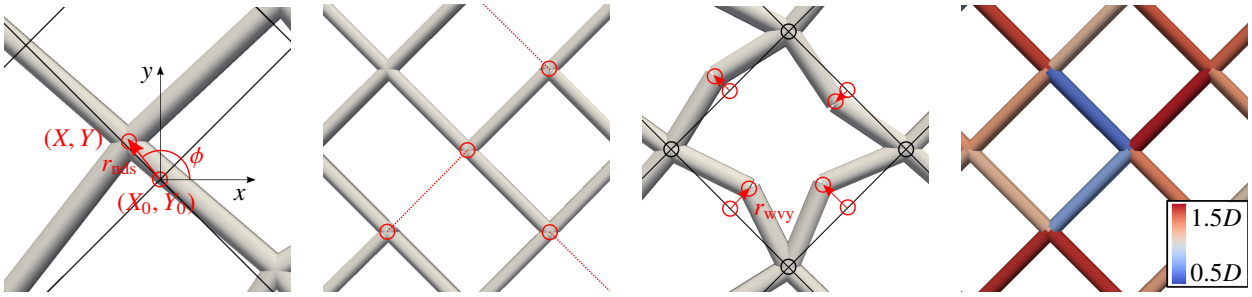

(a) **Node displacement** r_{nds} of the nominal node position over a statistically sampled distance r_{nds} and in a statistically sampled direction.

(b) **Missing beams** are realised by randomly removing beams within the lattice. In simulations the same effect is achieved by reducing those beams' Young's moduli to small values.

(c) **Wavy beams** are approximated by moving a beam's midpoint onto the circumference of a circle perpendicular to the beam and of radius r_{wvy}, based on statistical sampling.

(d) **Diameter variations** along the beam length let the diameter d follow a Gaussian distribution centered at the nominal diameter D and with standard deviation $\sigma = \xi_{\text{dia}} D$.

Figure 2: Visualization of imperfection types in 2D. In (a) and (c), the solid black lines show the original, undeformed lattice. The color code in (d) visualizes the different diameters.

considered to be broken. Throughout all of the following examples, we restrict $\xi_{\text{nds}} < 0.2$, as more than 20% of beams missing can no longer be considered as an 'imperfection' and also makes simulations and experiments complicated to realize.

- **Beam waviness:** although as-designed trusses typically feature straight beams, as-manufactured struts often show waviness [14], which is induced, e.g., by mechanical vibrations or layering steps during 3D-printing. Parameter $\xi_{\text{wvy}} \in [0, 1]$ quantifies the maximum positional deviation of a beam centerline from its straight nominal configuration, as shown in Figure 2(c). In simulations, this imperfection is realized by introducing an additional node at the center of the beam at a distance r_{wvy} from the beam's longitudinal axis and the beam's midpoint, as shown in Figure 2(c). For a statistical distribution, the new node's position is chosen from a circle in the plane perpendicular to the beam centerline and centered on the beam's midpoint (Figure 2(c)). The displacement r_{wvy} is obtained form a half-Gaussian distribution centered at $\mu = 0$ and having the standard deviation $\sigma = \xi_{\text{wvy}} L$. The new node's location on the circle is defined by a uniformly distributed angle $\zeta \in [0, 2\pi]$. Of course, wavy beams in reality can assume complex shapes not represented here; however, the proposed kink is a straightforward approximation efficiently capturing the loss in axiality of a beam. We impose $\xi_{\text{wvy}} < 0.1$ to prevent contact between beams (and also because larger imperfections may not be viewed as "imperfections" anymore but rather present a change in design).

- **Diameter variation:** 3D-printing often causes substantial erroneous variations in the cross-section of a beam along its length [6, 16, 36, 39, 40], as illustrated in Figure 2(d). In the following, we select a circular cross-section for the study of different topologies in Section 4, while comparison to experiments in Section 5 will

require the use of elliptical cross-sections. For circular cross-sections, the diameter of the beams in the RVE is described either by a normal Gaussian distribution centered at $\mu = D$ with standard deviation $\sigma = \xi_{\text{dia}} D$, where D is the nominal diameter and $\xi_{\text{dia}} \in [0, 1]$ controls the diameter variations, or by a half-Gaussian distribution with the analogous features. The imperfect cross-section of each beam is obtained from the new diameter d generated by the Box-Muller transform. (For elliptical cross-sections, the analogous holds, with variations being applied to the major axes of the ellipse.) We study both normal Gaussian (Section 5) and half-Gaussian (Sections 3 and 6) distributions in response to the different fabrication techniques. The two-photon lithography used in our experiments leads to beams being thinner or thicker than nominal, while experiments that used Selective Laser Sintering (SLS) observed that the diameter only increases from its nominal value [14]. This also underlines the versatility of the model, as it applies to different imperfection distributions, as needed for a particular application or fabrication route. Here, we impose $\xi_{\text{dia}} < 0.2$, since we consider larger imperfections as design choices rather than defects. (We note that one could also consider variations of beam diameters along the length of a strut. Yet, for simplicity we consider constant cross-sections per strut (in reality, the strength of a given strut is typically determined by its thinnest cross-section.)

3. Homogenized stiffness of imperfect trusses

The numerical study of imperfections is realized using a fully resolved RVE with purposely introduced imperfections, described by ξ_{nds} (node displacements), ξ_{mis} (missing beams), ξ_{wvy} (wavy beams), and ξ_{dia} (diameter variations). The impact of the four defect types is assessed by comparing the effective stiffness of an imperfect truss with that of a perfect truss. We define the defect *sensitivity* of a truss topology as the ratio of the normalized effective moduli with respect to those of the defect-free truss. We simulate each (perfect and imperfect) truss as an assembly of linear elastic Euler-Bernoulli beams with rigid nodal connections. Beams are chosen to be sufficiently slender (and trusses are consequently in the low-relative-density regime), so that Euler-Bernoulli beam theory is applicable, while the extension to Timoshenko beams is technically straightforward. We stress that the relative densities of the investigated lattices (and any derived quantities) are not adjusted for the presence of imperfections. Instead, we treat variations in density as a byproduct of an imperfection type. As such, variations in relative density are already implicitly included in the conclusions of our exploration.

While for periodic truss structures the effective response can be obtained by homogenizing a single representative unit cell [17, 32–34], this becomes impractical in the case of an imperfect truss. The latter breaks the periodicity of the truss and hence not only makes the choice of an RVE non-unique and challenging but also prevents the application of periodic boundary conditions.

Therefore, we compute the homogenized response of a sufficiently large RVE (containing many UCs) by applying affine displacement boundary conditions [41]. Due to the randomness of the introduced imperfections, we perform ensemble averaging and compute the average effective response over a number of equally large but random realizations

to ideally render the approach independent of domain size and imperfection distribution [42, 43]. To this end, we must choose the RVE, also referred to as SVE (stochastic Volume Element), significantly larger than an individual UC and the imperfections such that the resulting truss is statistically homogeneous (i.e., with uniform mechanical properties at larger scales). A discussion of the RVE size chosen in our study to satisfy these criteria is provided in Appendix B. We select the effective stiffness tensor $\bar{\mathbb{C}}$ as a representative measure to describe the mechanical response of an imperfect lattice. We follow the common approach of applying six linearly independent 3D strain cases (three cases in 2D) through affine displacement boundary conditions on the outer boundary of the RVE and computing the resulting average stress tensors within the RVE. Correlating stresses and strains yields the full 3D (or 2D) stiffness tensor components [18, 44].

We restrict our study to topologies with cubic symmetry, which results in three independent material constants to be extracted from the effective stiffness tensor $\bar{\mathbb{C}}$; e.g., the effective Young's modulus $\bar{E}$, the effective generalized Poisson's ratio $\bar{\nu}$, and the effective shear modulus $\bar{G}$, which characterize, respectively, the uniaxial stiffness, the Poisson effect, and the shear resistance of the truss.

These are conveniently obtained form the compliance tensor $\bar{\mathbb{S}} = \bar{\mathbb{C}}^{-1}$ in Voigt notation [45]:

$$\begin{aligned} \bar{E} &= (1/\mathbb{S}_{11} + 1/\mathbb{S}_{22} + 1/\mathbb{S}_{33})/3, \\ \bar{\nu} &= (\mathbb{S}_{12}/\mathbb{S}_{11} + \mathbb{S}_{13}/\mathbb{S}_{11} + \mathbb{S}_{23}/\mathbb{S}_{33})/3, \\ \bar{G} &= (1/\mathbb{S}_{44} + 1/\mathbb{S}_{55} + 1/\mathbb{S}_{66})/3. \end{aligned} \tag{2}$$

For each truss topology and for each combination of the statistical defect parameters $(\xi_{\text{nds}}, \xi_{\text{mis}}, \xi_{\text{wvy}}, \xi_{\text{dia}})$ we create N random realizations of sufficiently large RVEs (see Tables 3 and 4) and determine the elastic moduli in (2) as the ensemble averages over the N realizations.

For defect-free trusses, a single realizations is, of course, sufficient, whose computed effective moduli (with the chosen RVE sizes and affine displacements boundary conditions) agree well with the homogenized moduli obtained form a single UC with periodic boundary conditions [33] (see Appendix A).

We study a representative selection of truss topologies in 2D (cross-squared, triangle, hexagon, square, diamond, kagome) and in 3D (octet, octahedron, bitruncated octahedron, cube, 3D diamond), which covers a broad range of properties from stiff, stretching-dominated structures with nodal connectivities $Z \geq 4$ in 2D and $Z \geq 6$ in 3D) to highly bending-dominated, compliant ones (with $Z < 4$ in 2D and $Z < 6$ in 3D) [46]. (Of course, the provided framework can also be applied to other topologies). While theoretically $\xi \in [0, 1]$, in reality a truss becomes impossible to print or difficult to simulate above a certain ξ-value (and we cannot really interpret the truss as a periodic network with imperfections anymore). We therefore restrict the range of ξ in the following parameter study to $\xi_{\text{nds}} \in [0, 0.3]$, $\xi_{\text{mis}} \in [0, 0.2]$, $\xi_{\text{wvy}} \in [0, 0.1]$ and $\xi_{\text{dia}} \in [0, 0.2]$. For ease of comparison, we assign to all structures the same beam slenderness ratio $\lambda = D/L = 0.1$, which constitutes the lower limit for many 3D-printers when fabricating large samples while satisfying the Euler-Bernoulli assumption of slender beams [47]. Note that this results in varying relative densities (or fill fractions) across the chosen topologies, as shown for the 2D topologies in Table 3 and for the

3D topologies in Table 4. In 2D the relative density is computed as the ratio of the beam volume V_b to the total area of the RVE, A_{UC}, while in 3D we report the relative density (i.e., the fill fraction).

	Cross-square	Triangle	Hexagon	Square	Diamond	Kagome
Topology			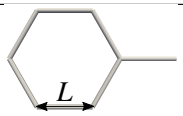	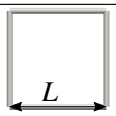	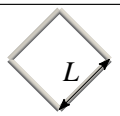	
RVE size	100×100	100×58	67×116	100×100	100×100	100×58
V_b/A_{UC}	$\frac{1+\sqrt{2}}{2}\frac{D^2\pi}{L}$	$\frac{\sqrt{3}}{2}\frac{D^2\pi}{L}$	$\frac{\sqrt{3}}{6}\frac{D^2\pi}{L}$	$\frac{1}{2}\frac{D^2\pi}{L}$	$\frac{1}{2}\frac{D^2\pi}{L}$	$\frac{\sqrt{3}}{4}\frac{D^2\pi}{L}$
λ	0.1 (0.14)	0.1	0.1	0.1	0.1	0.1
Z	8 (4)	6	3	4	4	4

Figure 3: The six truss topologies studied **in 2D** along with the chosen RVE size (in UCs), relative area density V_b/A_{UC}, slenderness ratio λ, and nodal connectivity Z. The RVE size is defined as the number of UCs (a single UC is shown in each case) tessellated along the two principle axis to build the full RVE. In all topologies, all respective beams have the same length with a fixed slenderness ratio of $\lambda = 0.1$—except for the shorter struts in the cross-square topology, where we used $\lambda = 0.14$.

	Octet	Octahedron	Bitr. Oct.	Cube	Diamond 3D
Topology	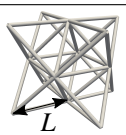	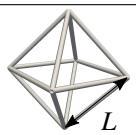	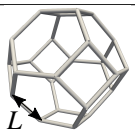	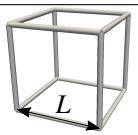	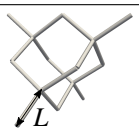
RVE size	$30 \times 30 \times 30$	$30 \times 30 \times 30$	$40 \times 40 \times 40$	$30 \times 30 \times 30$	$30 \times 30 \times 30$
V_b/V_{UC}	$\frac{3\sqrt{2}}{2}\pi\frac{D^2}{L^2}$	$\frac{3\sqrt{2}}{4}\pi\frac{D^2}{L^2}$	$\frac{3}{16}\sqrt{2}\pi\frac{D^2}{L^2}$	$\frac{3}{4}\pi\frac{D^2}{L^2}$	$\frac{\sqrt{2}}{8}\pi\frac{D^2}{L^2}$
λ	0.1	0.1	0.1	0.1	0.1
Z	12	8	4	6	4

Figure 4: The five truss topologies studied **in 3D** along with the chosen RVE size (in UCs), relative density V_b/V_{UC}, and nodal connectivity Z. The RVE size is defined as the number of UCs (a single UC is shown in each case) tessellated along the three principal axes to build the full RVE. The slenderness ratio is fixed as $\lambda = 0.1$.

4. Homogenization results: imperfection sensitivity of the effective stiffness

Figures 5 and 6 summarize the homogenized effective elastic properties of the studied truss topologies in 2D and 3D, respectively, as functions of the four statistical defect distributions introduced in Section 2.

Error bars indicate the standard deviation obtained from $N = 100$ random RVE realizations for each choice of ξ_i. As may be expected, the shown standard deviations increase with increasing ξ_i-values. Results show that the defect

sensitivity strongly depends on the truss topology and on the elastic property. For example, the effective Young's modulus of the square, kagome, and cube are highly sensitive to imperfections. By contrast, the triangle's effective Poisson's ratio $\bar{\nu}$ shows only a negligible sensitivity. We have not included the sensitivities of Passion's ratio $\bar{\nu}$ for the square and cube lattices in the plot, since the their values for a structure without any imperfections, $\bar{\nu}(\xi = 0)$, is negligibly small and can therefore not be used to reasonably compute the sensitivity. In agreement with previous findings [17], we observe a higher sensitivity of the kagome lattice to all types of imperfections as compared to a triangular topology. Across all topologies, the sensitivity of Poisson's ratio, $\bar{\nu}$, to variations in the beam diameter is almost negligible compared to the other three defect types. Also remarkable is the high similarity of the sensitivity of Young's modulus $\bar{E}$ of the square and kagome topologies under the influence of every geometrical imperfection. The same agreement is also observed for the shear modulus $\bar{G}$ of the diamond and kagome topologies. Let us discuss the specific influence of each type of imperfection.

Nodal displacements effect significantly the effective Young's moduli $\bar{E}$ of the highly anisotropic trusses, such as the square and cubic lattices, whose moduli drop on average by around 50% for $\xi_{\text{nds}} = 0.3$ (Figures 5a and 6a). By contrast, Young's moduli of the (bending-dominated) bitruncated octahedron and 3D diamond truss remain nearly unaffected by nodal displacements, owing to their low nodal connectivity, which is not influenced by the imperfections. Additionally, highly stretching-dominated topologies such as the cross and triangular trusses in 2D and the octet in 3D remain widely unaffected by increasing node displacements. Recall that we report the effective Young's modulus in the three principal directions. Therefore, structures with beams that are nominally aligned with the principal directions (such as the square and cubic trusses) are highly sensitive to variations in nodes position, as this type of imperfection will result in a breaking of symmetry and a transition from stretching to bending mechanisms when loaded along the principal directions. Moreover, the shear modulus $\bar{G}$ of those structures with a relatively low nodal connectivity Z, which have beam connections under $\pi/4$ with respect to the principal cubic axes of the truss (such as in the diamond, kagome, and octahedron lattice) are highly sensitive to nodal displacements (Figures 5i and 6i). Displacing the nodes breaks the alignment of the force chains under shear and hence reduces the shear stiffness. The same applies to making the beams wavy, see Figures 5k and 6k. We note that, although the differences in nodal connectivity Z between the various truss topologies helps explain some of the observed effects, it cannot alone explain entirely the reported findings, which warrants further investigation.

Interestingly, structures that show little resistance to shear in their defect-free configuration, such as the hexagon, square, cube, and 3D diamond, display shear stiffening with increasing nodal displacements, as visualized in Figure 7. This remarkable feature is explained in Figure 8, which compares the shear deformation of a perfect cube truss to that of an imperfect one, having considerable node displacements with $\xi_{\text{nds}} = 0.3$. For improved visibility, we apply an extreme shear deformation of 10%, which does not affect the conclusions. The perfect truss (Figure 7a) distributes the load homogeneously, and the struts (oriented under 45° with respect to the principal load directions) deform primarily in bending and carry low stresses. This is turn yields a low resistance to shear. As ξ_{nds} increases (Figure 7(b)), an increasing number of beams tend to align with the principal directions, which leads to the apparent force chains (often

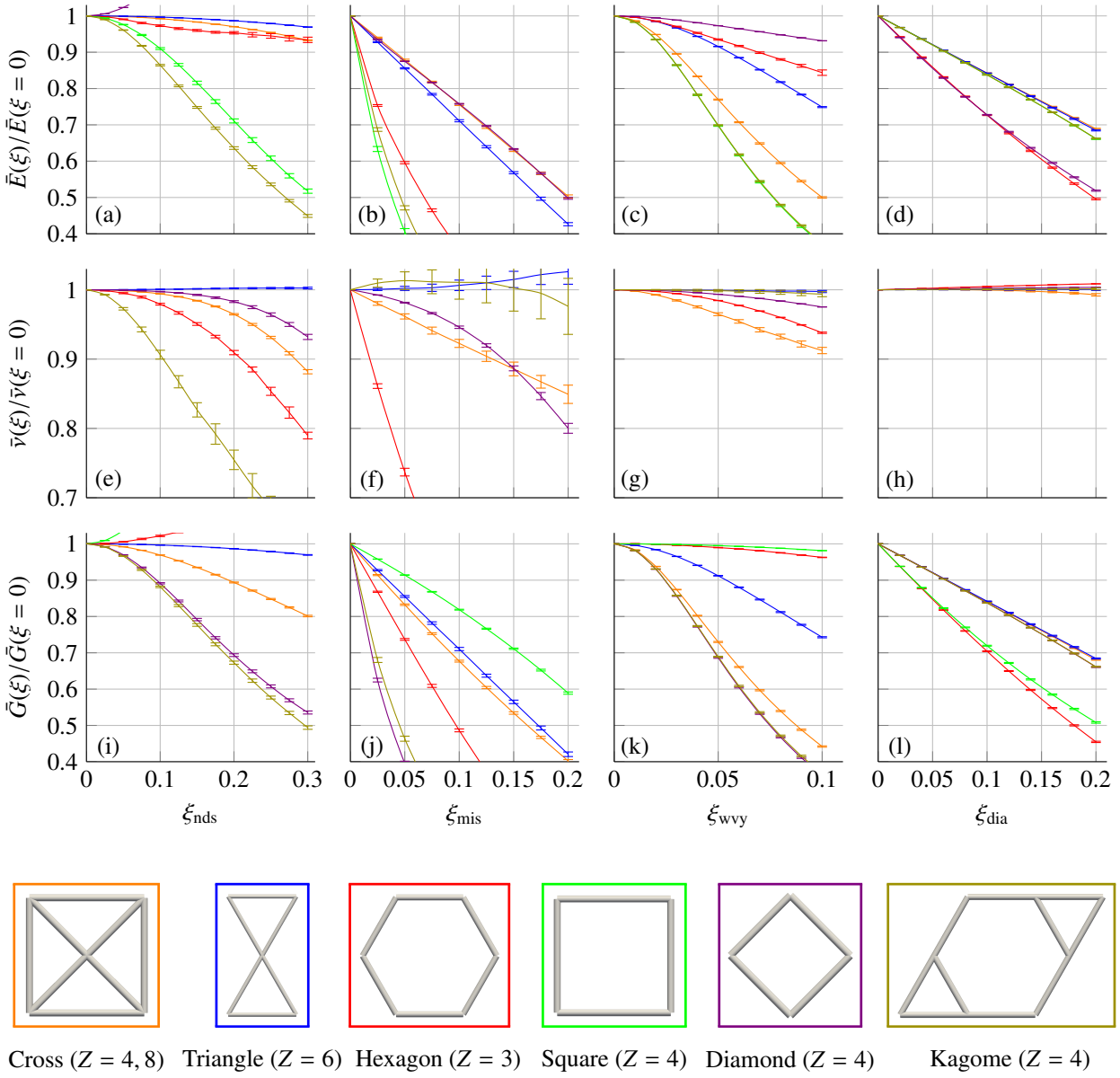

Figure 5: Sensitivity of **2D** bending- and stretching-dominated truss topologies with respect to the imperfection standard deviations ξ_{nds}, ξ_{wvy}, ξ_{dia}, and missing beam probability ξ_{mis}. Each error bar represents the standard deviation obtained from $N = 100$ random realizations of the imperfect trusses. Line and marker colors correspond to the six truss topologies shown below. While all nodes in any of the structures have the same coordination number of connecting struts, Z, the cross unit cell has two type of nodes, connected to different numbers of struts, which is why the coordination number for some nodes in the cross lattice is $Z = 4$, while for others $Z = 8$.

observed in granular materials [48]) with high tensile and compressive stresses in the two principal directions.

The same explanation holds for the increase in Young's modulus of the 2D diamond lattice when subjected to node displacements (Figure 5a)—with the only difference that the loading direction and topology are rotated by 45°

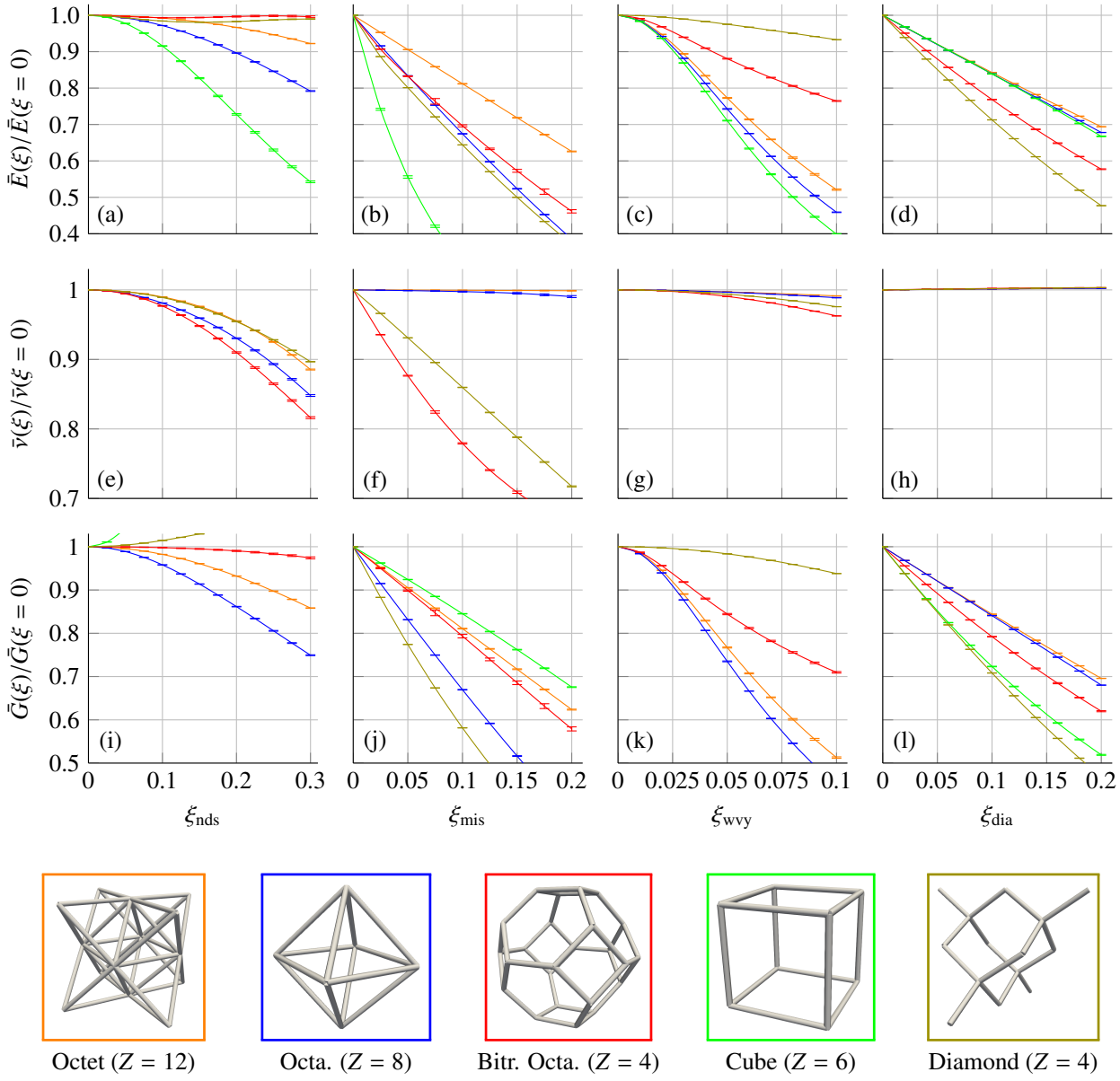

Figure 6: Sensitivity of **3D** bending- and stretching-dominated truss topologies with respect to the imperfection standard deviations ξ_{nds}, ξ_{wvy}, ξ_{dia}, and missing beam probability ξ_{mis}. Each error bar represents the standard deviation obtained from $N = 100$ random realizations of the imperfect trusses. Line and marker colors correspond to the five truss topologies shown below.

to the above case. Again, increasing ξ_{nds} leads to force chains along the principal loading directions and hence to a stiffening of the structure, which transforms from bending- to stretching-dominated.

Missing beams reduce the rigidity and promote bending in the truss, significantly reducing the effective stiffness [49] as well as its yield strength [50]. As there is an extensive body of prior work on missing beams in 2D and 3D

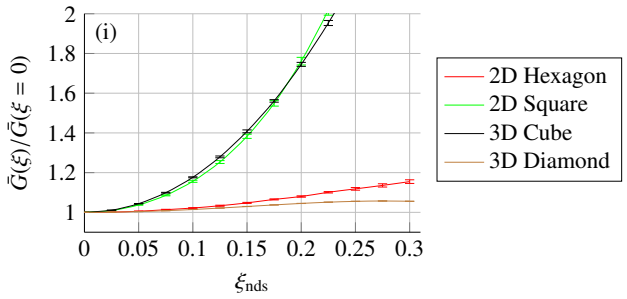

Figure 7: Variations of the effective **shear modulus** $\bar{G}$ of the 2D hexagonal and square, and the 3D cube and diamond topologies with increasing nodal displacements (as a function of the standard deviation ξ_{nds} of the node displacement distribution).

trusses, we may use that data for a validation of our homogenization setup (which is presented in Appendix C). Our results confirm a severe impact of missing beams on the effective Young's modulus of those structures with low nodal connectivity Z, such as the 2D hexagonal ($Z = 3$) and square lattices ($Z = 4$), and the corresponding 3D topologies, i.e., the bitruncated octahedron ($Z = 4$) and cubic ($Z = 6$) topologies (Figures 5b and 6b). A connection between the nodal connectivity (related to the predominant deformation mode) and missing connections was already reported in previous studies [17] as the main factor behind the reduction of the effective Young's modulus of truss metamaterials. The higher the number of beams connected at a node, the better the load is redistributed on the surrounding beams if one of them is missing, keeping the structure stretching-dominated. Similar to the reported sensitivity of Young's modulus with increasing nodal displacements (Figures 5a and 6a), structures that take the loads applied in the three principal cubic directions by beams aligned with those directions (e.g., the square and cube) lose a significant amount of their stiffness in those directions when the perfect beam alignment is broken by imperfections. Interestingly, the diamond, even though a bending-dominated topology, is as resistant to missing beams as the highly stretching-dominated cross lattice. This underlines that the nodal connectivity Z can explain many but not all observations. For trusses with higher nodal connectivity (triangular, cross, and octet lattices), a moderate reduction of $\bar{E}$ and $\bar{G}$ is observed, as the fraction of missing beams increases. Their effective Poisson's ratio $\bar{\nu}$ is marginally affected by this imperfection. By contrast, for low Z and with an increasing number of missing beams, large unconnected regions (i.e., voids) form across the structure, causing high stress concentrations and promoting failure. This observation agrees with previous research that focused on the impact of missing beams on the octahedron, bitruncated octahedron, and other 3D architectures [24].

Beam waviness generally leads to increased beam bending at the expense of beam stretching. Consequently, structures like the square, kagome, and cross lattice in 2D and the cubic lattice in 3D (whose beams align with the three cubic axes) are highly affected by the presence of wavy beams [14] (Figures 5c and 6c). On the other hand, bending-dominated structures such as the hexagonal, diamond or bitruncated octahedron lattices are the least affected by wavy beams and only show minor reductions of their effective Young's modulus [17]. Note that we focus on the effective elastic response and do not consider the increased risk of buckling of members in compression, which may

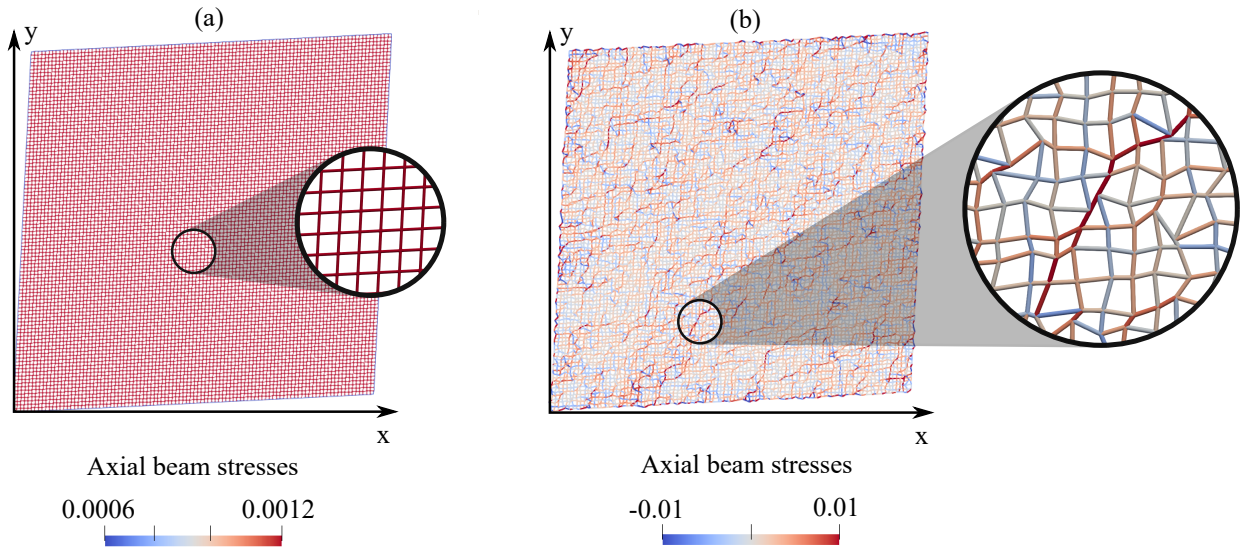

Figure 8: Comparison of the **2D** ideal square RVE on the left and the respective non-ideal counterpart with strong nodal displacement imperfections $\xi = 0.3$ on the right. For visualization purposes, we here increase the shear strain to $\varepsilon_0 = 10\%$ and highlight the axial stresses in every beam element, normalized by the materials Young's modulus E. Inside the imperfect lattice force chains develop (emphasized in the circular magnification), corresponding to axial tensile stresses in the direction of loading and axial compressive stresses perpendicular to it.

significantly reduce the strength of the structure.

Variations of the cross-sectional area show a similar trend of the effective properties for all studied topologies: $\bar{E}$ decreases steadily with increasing diameter variations, while Poisson's ratio $\bar{\nu}$ is only marginally affected. All topologies show a steady decrease of $\bar{G}(\xi)$, with the bending-dominated hexagon and 3D diamond lattice being the most sensitive to beam diameter changes. (Note that considering diameter variations larger than nominal—here they are confined to consider only diameter reductions—may lead to a different sensitivity towards this imperfection.)

5. Experiments

To confirm the accuracy of the model described above, we performed experiments on 3D-printed octahedron trusses as a representative 3D example. For a fair comparison between simulations and experiments, we modified the numerical setup to match the experimental conditions in terms of sample size, boundary, and loading conditions. We computationally design imperfect trusses with intentional defect distributions, and probe their effective stiffness under uniaxial compression using both simulations and experiments (see Figure 9).

5.1. Nanomechanical Experiments

We performed quasi-static nanomechanical compression experiments (Alemnis ASA) on a $5 \times 5 \times 5$ octahedron lattice with clamped boundaries at the bottom and top (Figure 10). We chose fabrication at the microscale, using a

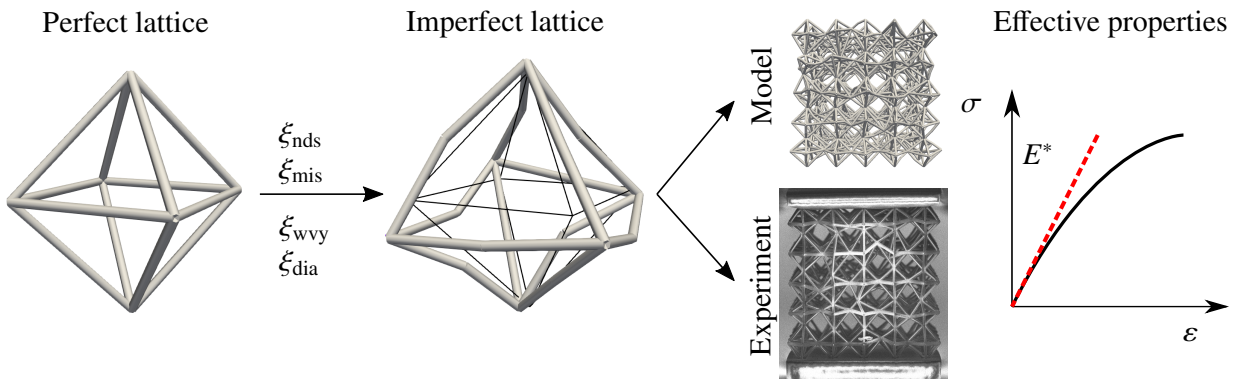

Figure 9: Protocol for comparing simulated with experimentally determined stiffness data: after applying imperfections to a *defect-free* lattice, the effective response of the truss is obtained from the stress-strain curve under uniaxial compression—both from simulations and from experiments on a 3D-printed truss.

two-photon lithography system (Nanoscribe GmbH, Ip-Dip photoresist), due to its high resolution and the ability to print slender structures, for which the beam theory approximation is valid [51, 52]. The dimensions of the lattices were $130 \times 130 \times 130$ µm^3, resulting in a constant beam length of ~18 µm. We first printed *defect-free* lattices (within the tool's tolerances), which served as a reference for the computation of the sensitivity to geometric imperfections. The fabricated beams possessed an elliptical cross-section with an average major axis of $a = 2.3 \pm 0.1$ µm and a minor axis of $b = 1.8 \pm 0.1$ µm. Due to limitations in the printing process, the ratio between the major to minor axis varied linearly from ~1.3 to 1 between horizontal struts and vertical struts, which was accounted for in the numerical models. The elliptical shape of the diagonal and horizontal beams is a consequence of the chosen printing process close to the resolution limit. The overall dimensions of the fabricated samples remained negligibly affected by shrinkage in the

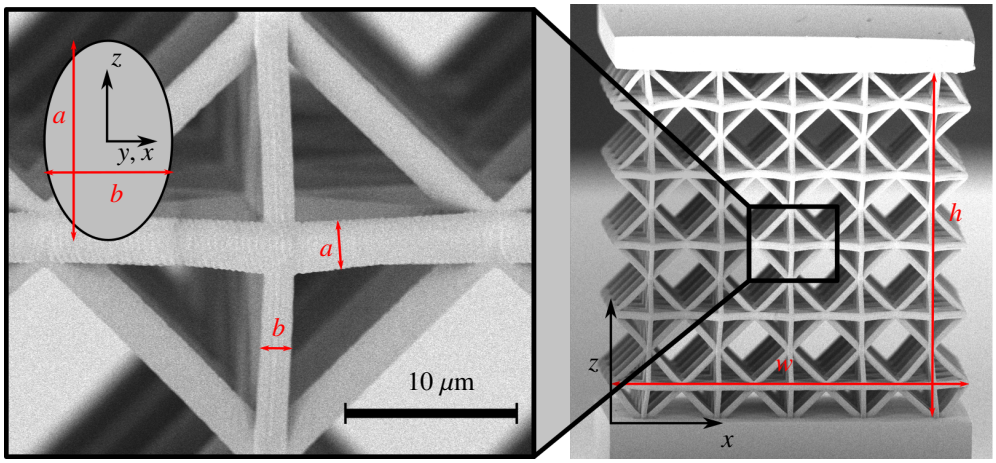

Figure 10: Representative sample with no imperfections (*defect-free*) in its pre-loading state. The inset highlights the elliptical beam cross-sections.

development process, resulting in an overall sample width $w \sim 130 \pm 2$ µm and height $h \sim 130 \pm 2$ µm, as shown in Figure 10. The cross-sectional area of each elliptical beam was $A_e = \frac{\pi ab}{4}$ and the second moments of inertia $I_y = \frac{\pi}{64} a^3 b$ and $I_z = \frac{\pi}{64} b^3 a$.

Perfect and imperfect samples were produced by converting the beam models of Section 2 into Standard Tessellation Language (STL) format with finite beam thickness; i.e., we deliberately 3D-printed perfect and imperfect samples with as-design defect distributions of the four types discussed above. In the case of diameter imperfections, both major axes a and b were multiplied by the same ξ_{dia}. When including missing beams, beams on boundaries of the truss were excluded from being removed to avoid boundary nodes from being only partially supported. Similarly, boundary nodes at the top and bottom clamps were excluded from the node-displacement imperfection to prevent disconnections from the supporting plates. In the case of diameter variations, we continue to use a Gaussian distribution to vary ξ_{dia}; however, we restrict the random diameter to not fall beneath 2/3 of its nominal value (i.e.,

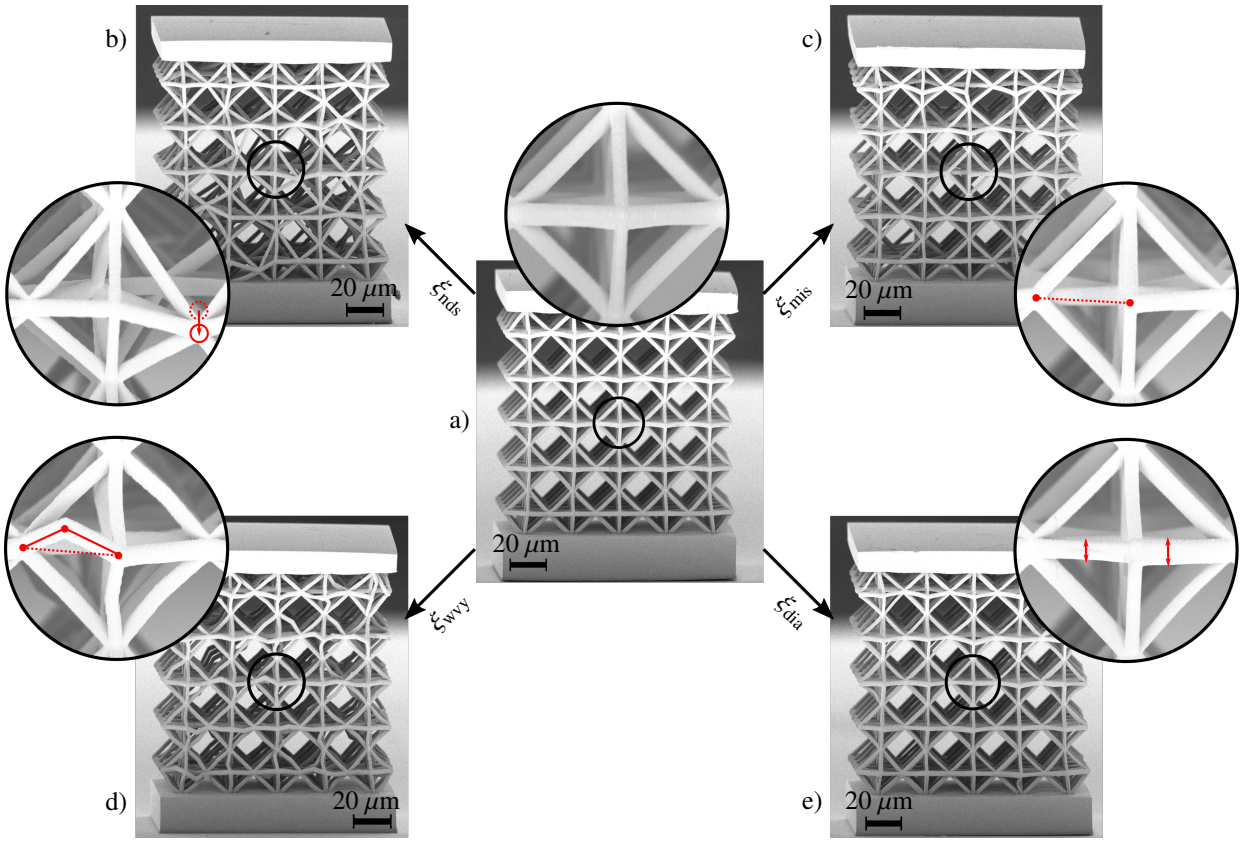

Figure 11: Visualisation of all four imperfections types which were intentionally included in the truss samples. The center image a) shows the *defect-free* octahedron lattice. In the corners, we visualize the four different imperfection types applied to the perfect lattice with b) showing *node deviations*, c) *missing beams*, d) *wavy beams* and e) *diameter variations*. We additionally zoom into a section of each lattice and highlight the imperfection in red.

$a > 1.2$ µm for the elliptical cross-section) to honor the print limitations. As already explained in the introduction, we additionally allow the diameter to increase (according to a Gaussian distribution), since with two-photon lithography, Stereolithography (SLA), or Digital Light Processing (DLP), beams may also end up thicker than nominal. Figure 11 provides a visualization of all four types of imperfection in printed samples. The magnitude of each imperfection was chosen to exceed the fabrication tolerances of the two-photon lithography technique by orders of magnitude, so that fabrication-induced imperfections play only a minor role (which also confirms the choice of this printing process to be ideal for this study).

5.2. Modeling the experimental conditions

In Section 3 we reported homogenized elastic properties, which admitted general insight into the effective truss performance and have classically been reported. Here, by contrast, we change the simulation setup to match the experimental conditions. To this end, we simulate the uniaxial compression of samples that are fully clamped on the top and bottom faces with free lateral faces. Instead of simulating large RVEs, we model samples of $5\times5\times5$ UCs as in experiments. Moreover, beam cross-sections have the same elliptical shapes as in experiments. The elastic properties of the base material used in simulations were obtained from compression experiments on micropillar produced with identical printing conditions as the trusses. We extract the effective Young's modulus E^* of truss samples in the compression direction from the slope of the stress-strain curve. As before, we compute the average response of $N = 100$ random realizations for a given set of imperfection distributions.

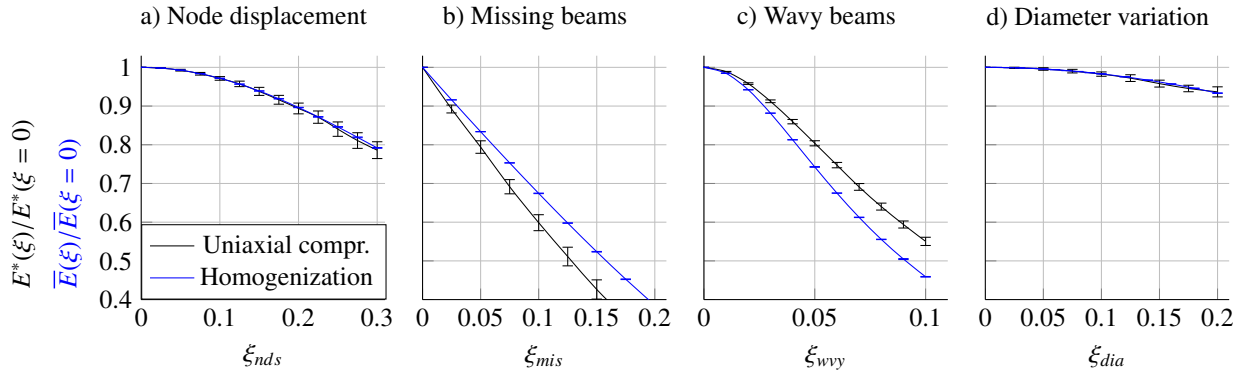

Figure 12: Comparison of the sensitivity of the effective Young's of an octahedron truss with respect to three different types of imperfections, as obtained from homogenization and from uniaxial compression. For the comparison between uniaxial compression and homogenization, we choose a $40\times40\times40$ octahedron lattice with beams having circular cross-sections, as shown in Figure 6. In cases (a) - (c), the results of the homogenization approach are identical to those of Figure 6, whereas for (d) the diameter variation now represents the same setting as for the experimental setup (diameters may be larger or smaller than nominal).

To illustrate the differences between the two loading scenarios, Figure 12 compares the effective Young's modulus of the octahedron truss with varying imperfection distributions, as obtained from homogenization (Section 3) and from uniaxial compression simulations. Although results differ quantitatively, the same qualitative trends are observed (in

the case of node displacement and diameter variation, both approaches yield nearly identical results). This indicates that, although the boundary conditions are different, the general conclusions drawn in Section 3 can also be expected to hold here.

5.3. Experimental results and comparison with simulations

Figure 13 shows the effective Young's modulus E^* (normalized by that of a defect-free truss) of trusses with four different types of imperfections. The imperfection strengths in this comparison study, $\xi_{\text{nds}} = 0.2$, $\xi_{\text{mis}} = 0.1$, $\xi_{\text{wvy}} = 0.1$, and $\xi_{\text{dia}} = 0.2$, are chosen to be relatively high to suppress the effects of any material imperfections. Each experimental data point represents the average of five experiments, each conducted on a different lattice realization with identical imperfection magnitudes. The respective numerical simulations are averaged over 100 random realizations, applying the same imperfection magnitude but not the exact same distribution as in the experiment. We refrained from comparing the experiment to a simulation with the exact same imperfection distribution to demonstrate the strength of the model to be generally applicable independent of the exact imperfection realization. Simulations generally over-predict the effective truss stiffness by an approximately constant offset, which we attribute to inevitable small imperfections in the printing and possibly a slightly different polymerization state between the truss samples and the micropillars used to calibrate the model (the effective stiffness of the defect-free truss differs by 11.8% between simulations and experiments). Furthermore, the print direction [14], node geometry [36, 53], node fillet size [54], and boundary effects can affect the mechanical response and hence contribute to the offset. Figure 13 confirms that the impact of the four types of defects shows excellent agreement between simulations and experiments. The relative error between those is 15.9% for displaced nodes, 25% in case of missing beams, 25.3% for wavy beams, and 22.8% for varying diameters. Overall, this confirms the successful prediction of the influence of imperfections by the model – and we use the close to constant offset of $\sim 20\%$ between the experimental and numerical data to introduce a correction factor of 1.2 to be used with all subsequent simulation data.

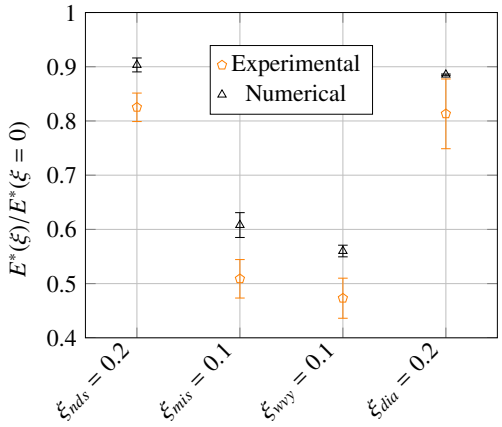

Figure 13: Comparison of the experimentally measured and simulated effective Young's moduli of four octahedron trusses, each with a different type of imperfection. Data are normalized with respect to the defect-free stiffness $E^*(\xi = 0) = 13.1$ MPa in the simulation and $E^*(\xi = 0) = 11.1$ MPa in case of the experiment. The shown standard deviations of the experimental data stems from averaging over five identical structures, while the standard deviation of the simulated data is the result from averaging over 100 different random realizations of the imperfections. (We refrain from comparing the experiment to simulations on the exact same defective truss to underline the generality of the model to accurately capture the experimental observations without knowing the exact defect distribution.

6. Predicting imperfections using inverse modeling

The model of Section 4 uses the defect distributions as input parameters to compute the resulting effect on the effective mechanical properties of imperfect trusses. We can also revert the problem and pose the inverse question. Can we devise a predictive tool, capable of providing information about the distribution of imperfections by using the measured mechanical response of a truss as the input? In the following, we apply this inverse strategy to two different scenarios, based on the previously described sensitivity calculations: Section 6.1 uses the rather hypothetical availability of 15 of the anisotropic homogenized effective elastic constants of a defective truss, as described in Section 3. Section 6.2 only uses three measurable input parameters, derived from the setup in Section 5, for which we also present experimental benchmarks.

6.1. Inverse model based on homogenized elastic constants

We create a general machine learning framework that takes as input an a-priori chosen set of effective mechanical properties (e.g., Young's moduli, Poisson's ratios, shear moduli) of imperfect topologies, and it outputs a probability distribution of the imperfections likely to cause the deviations in the observed mechanical properties from the ideal ones. Figure 14 shows a schematic of the approach based on conditional variational autoencoders (CVAE), whose methodological and training details are presented in Appendix D.

We consider the five 3D topologies shown in Figure 6, whose homogenization (as described in Section 3) yields their effective Young's moduli $\bar{E}$, effective Poisson's ratios $\bar{\nu}$, and effective shear moduli $\bar{G}$ – resulting in a total of 15 available material constants. As in Section 3, we use RVEs of $30 \times 30 \times 30$ UCs and circular beam cross-sections

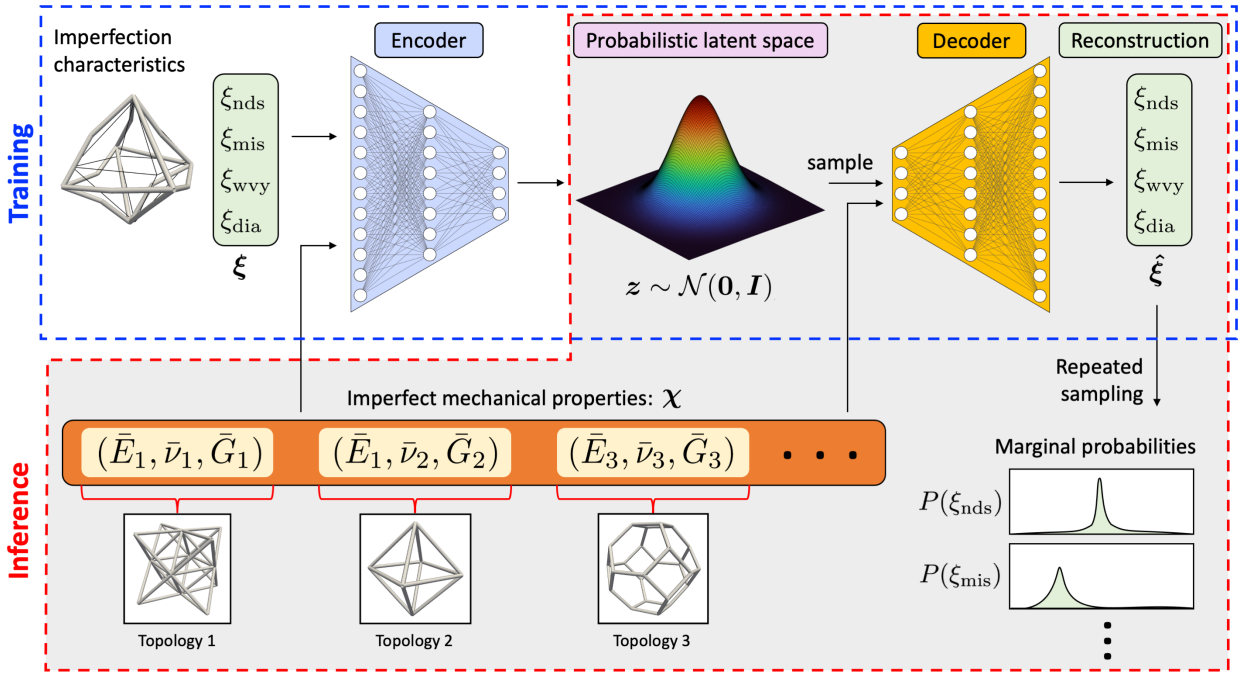

Figure 14: Setup of the Conditional Variational AutoEncoder (CVAE) used for the inverse prediction of an imperfection distribution based on effective elastic truss properties.

with a slenderness ratio of $\lambda = 0.1$ in simulations. Imperfections are randomly added from the ranges $\xi_{\text{nds}} \in [0, 0.3]$, $\xi_{\text{mis}} \in [0, 0.2]$, $\xi_{\text{wvy}} \in [0, 0.1]$, and $\xi_{\text{dia}} \in [0, 0.2]$. We generate a training dataset of 1215 different imperfection parameter combinations $\boldsymbol{\xi} = \{\xi_{\text{nds}}, \xi_{\text{mis}}, \xi_{\text{wvy}}, \xi_{\text{dia}}\}$ and compute the corresponding 15 homogenized elastic properties $\boldsymbol{\chi} = \{\bar{E}_1, \bar{\nu}_1, \bar{G}_1, \ldots, \bar{E}_5, \bar{\nu}_5, \bar{G}_5\}$ across the five topologies (Figure 6). For validation purpose, we also generate a similar test dataset containing 520 pairs of imperfection parameters $\boldsymbol{\xi}$ and elastic properties $\boldsymbol{\chi}$. The test dataset is not exposed to the machine learning model during the training stage. Using the training dataset, we train the aforementioned machine learning model (for details, see Figure 14 and Appendix D) with the objective of identifying the defect distribution $\boldsymbol{\xi}$ for given elastic properties $\boldsymbol{\chi}$. Rather than resulting in a unique defect values $\boldsymbol{\xi}$, the stochastic machine learning model predicts a joint probability distribution $P(\boldsymbol{\xi})$ (over all the four imperfection types in $\boldsymbol{\xi}$) which further quantifies the uncertainty of the prediction. Note that $P(\boldsymbol{\xi})$ is empirically obtained by repeatedly sampling a sufficiently large number of output predictions from the machine learning model. In the context of the following results, we use 3000 samples for each set of elastic properties input χ to obtain a representative probability distribution. (Each prediction is made almost instantly and therefore, the computational expense of repeated sampling is negligible).

To quantify the accuracy of the machine learning model, we compare the true imperfection parameters ($\boldsymbol{\xi}^{\text{true}}$) with the expectation of the marginal probabilities $\left\{\mathbb{E}[P(\xi_{\text{nds}})], \mathbb{E}[P(\xi_{\text{mis}})], \mathbb{E}[P(\xi_{\text{wvy}})], \mathbb{E}[P(\xi_{\text{dia}})]\right\}$ predicted for a given set of elastic properties $\boldsymbol{\chi}$. Note that the marginal probability distribution of a particular imperfection type is computed

by straightforwardly ignoring the other imperfection types in the collection of the joint samples of $\boldsymbol{\xi}$ predicted by the machine learning model, while the expectation $\mathbb{E}[\cdot]$ is approximated by the mean of those samples.

Figure 15 summarizes the accuracy between the true $\boldsymbol{\xi}$ and the predicted marginal expectations of all four imperfection types for each $\boldsymbol{\chi}$ in the test dataset. For all the imperfection types, the predicted marginal expectation of ξ is close to its true counterpart (coefficient of determination $R^2 \geq 98\%$), showing that our model is an accurate tool to predict defect distributions (and hence possible error sources, e.g., during the printing process). To further visualize the accuracy, we chose a random set of elastic properties $\boldsymbol{\chi}$ from the test dataset and compare its true imperfection parameters ξ with the predicted marginal probability distributions. A representative example is illustrated in Figure 16, which shows that not only is ξ predicted close to the actual values but also how our model provides a probability distribution quantifying the uncertainty. This feature becomes handy when applying the model to experimental data, where the measured effective properties always come with a measurement inaccuracy (as discussed below).

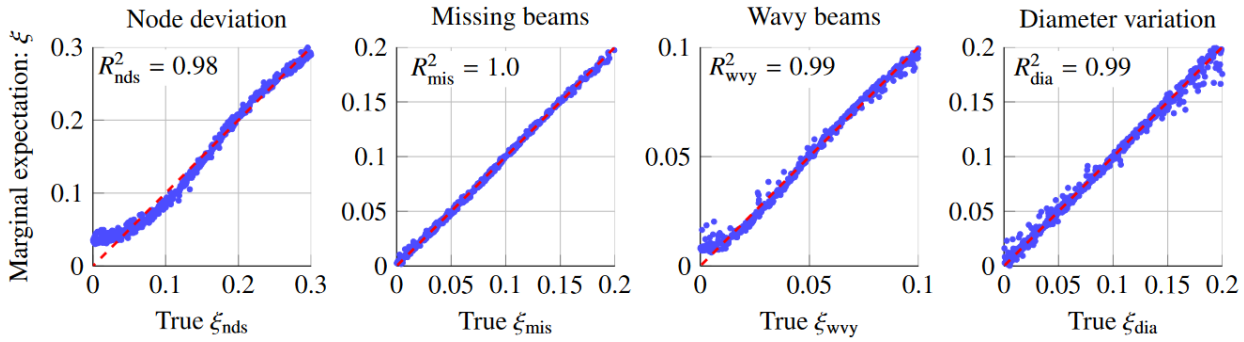

Figure 15: Accuracy of the predicted marginal expectation of each imperfection vs. the true value on the test dataset. All dashed lines (in red) represent the ideal line with zero intercept and unit slope; the corresponding R^2 deviations are indicated. All 15 elastic properties are considered as input to the machine learning model.

Figure 17 demonstrates in a "heat map" the correlation between the 15 effective elastic properties of the studied topologies and the four imperfection types. Areas marked in white (i.e., close to zero correlation) are deemed irrelevant for the results in Figure 15 and can therefore be excluded in future studies. It is apparent that the values of Poisson's ratio remain approximately unaffected by any diameter changes or beam waviness, whereas the Young's and shear moduli show little correlation with node displacements of most topologies (with the cube topology being an exception). These are interesting general insights into the impact of imperfections on the different elastic properties. In addition, this correlation matrix can advise future studies by removing topologies/elastic properties with little significance for the prediction accuracy, reducing the experimental costs required to characterize the imperfections (as also utilized in the following results).

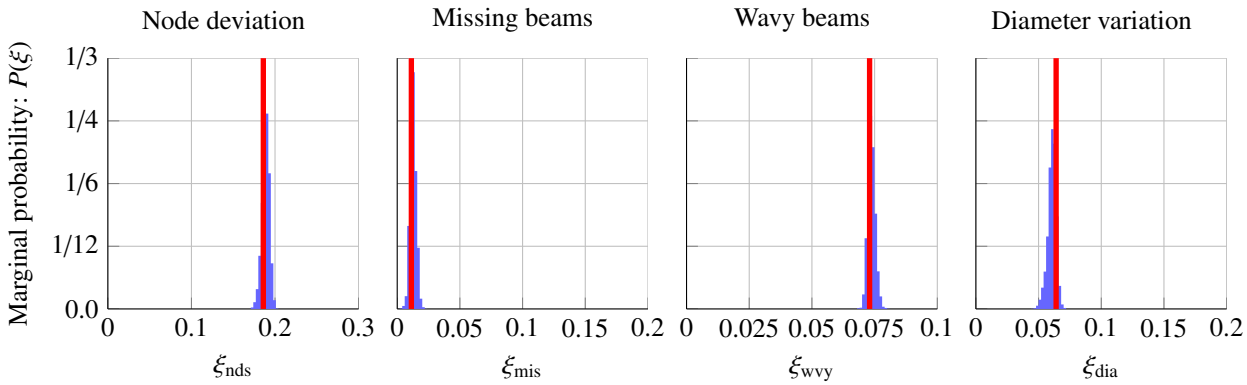

Figure 16: Predicted marginal probability distribution of imperfections for a sample chosen randomly from the test dataset with true imperfections $\xi_{\text{nds}} = 0.186$, $\xi_{\text{mis}} = 0.011$, $\xi_{\text{wvy}} = 0.073$, and $\xi_{\text{dia}} = 0.064$. Red lines shows the true values, while the blue distribution presents the marginal probability distribution of the predicted imperfections.

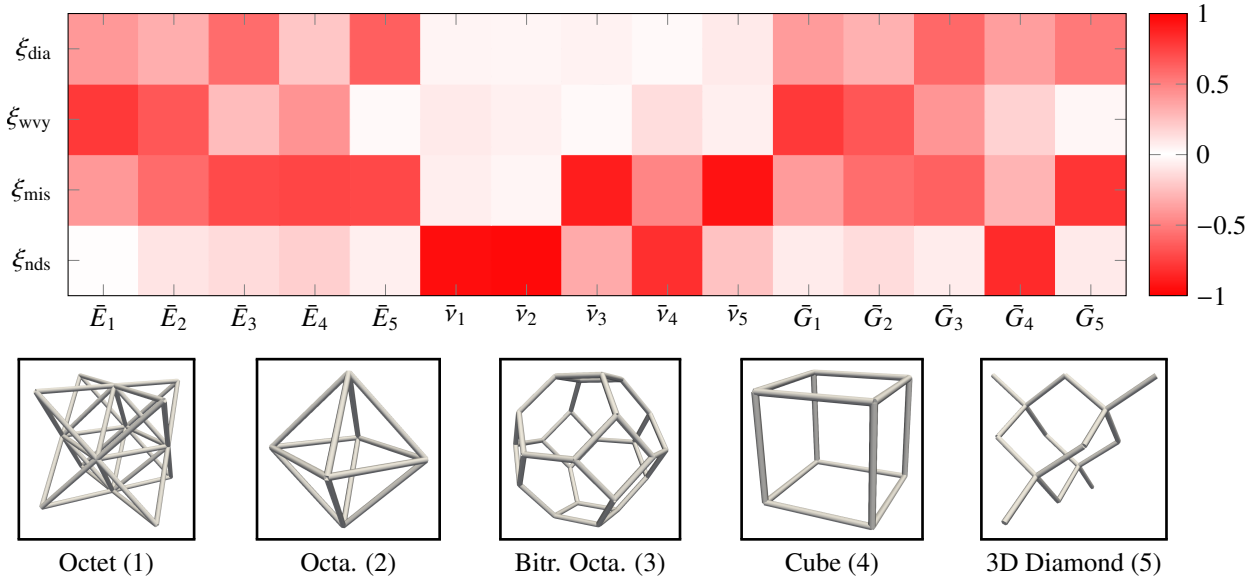

Figure 17: The "heat map" visualizes correlation coefficients between the effective elastic properties ($\bar{E}$, $\bar{V}$, $\bar{G}$) of the 3D truss topologies and the four imperfection types. A correlation coefficient of +1 or −1 indicates perfect correlation, while a value of zero may (or may not) indicate independence between two variables (positive or negative, respectively). Strong correlations are visualized in red, while input parameters with weak effect on ξ tend to a white color. Indices of the elastic properties correspond to the topologies shown below: 1) octet, 3) octahedron, 4) bitruncated octahedron, 4) cube, 5) diamond.

6.2. Inverse model based on uniaxial stiffness measurements

Of course, printing and testing five separate truss topologies to predict any printing-induced imperfections is unrealistic, considering the high cost and work load. In particular, experimentally determining Poisson's ratio and the

shear modulus of a truss is time-consuming and requires a complex setup, unlike the simple characterization of the uniaxial Young's modulus (see Section 5). We therefore adjust the machine learning framework of Section 6.1 to be applicable to standard experimental measurements. To this end, we use the same setup as in Section 5 and only consider the effective Young's modulus E^* of the five 3D truss topologies. Since we only increase (and not decrease) the diameter of beams imperfect, we can fabricate a *defect-free* lattice with thinner beams than in the experimental study of Section 5. The thinner beams are required to ensure a small slenderness ratio for the additionally printed bitruncated octahedron lattice, which has shorter beams than the octahedron. Printed beams have an elliptical cross-section with an average major axis of $a = 1.9 \pm 0.1$ µm and a minor axis of $b = 1.6 \pm 0.1$ µm. All other dimensions remain the same as in Section 5. We use the same elliptical beam dimensions for the initial defect-free lattice in our simulations. We again train a machine learning model with the analogous CVAE structure of Figure 14, now using only the five input parameters $\{\bar{E}_1, \bar{E}_2, \bar{E}_3, \bar{E}_4, \bar{E}_5\}$ instead of the previous 15 elastic properties to predict ξ. Imperfections are randomly chosen from the ranges $\xi_{\text{nds}} \in [0, 0.3]$, $\xi_{\text{mis}} \in [0, 0.2]$, $\xi_{\text{wvy}} \in [0, 0.1]$, and $\xi_{\text{dia}} \in [0, 0.2]$. Owing to the reduced computational costs, we choose a larger training set of $\sim$ 8166 trusses with randomly chosen imperfection distributions. We also generate a similar test dataset of 3500 trusses for validation purpose.

The accuracy of this new model on the test dataset reduces the coefficients of determination to $R^2_{\text{nds}} = 0.36$, $R^2_{\text{mis}} = 0.92$, $R^2_{\text{wvy}} = 0.97$, and $R^2_{\text{dia}} = 0.84$. By considering the quite varying correlations between elastic properties and imperfections (see Figure 17), we further reduce the number of topologies to three—retaining only the octet, bitruncated octahedron, octahedron—while obtaining almost the same prediction accuracy ($R^2_{\text{nds}} = 0.08$, $R^2_{\text{mis}} = 0.92$, $R^2_{\text{wvy}} = 0.96$, and $R^2_{\text{dia}} = 0.64$). The size of the training set was $\sim$ 10500, compared to 4500 trusses in the test set. We accept the $\sim$ 24% loss in R^2_{dia} due to the reduction of the tested topologies from five to three, since the extra workload of producing those is not worth the additional accuracy. The accuracy of predicting the node deviation ξ_{nds} was already low at 36%, so the further reduction to 8% is irrelevant at this point (we accept that ξ_{nds} cannot be predicted accurately based on this choice). However, by making these simplifications, we have reduced the complexity of the problem to three input parameters $\{\bar{E}_1, \bar{E}_2, \bar{E}_3\}$, facilitating a reasonable prediction of ξ_{mis}, ξ_{wvy}, and ξ_{dia}, as shown in Figure 18. By constrast, we can no longer predict node displacements (ξ_{nds}). However, the imperfections due to missing beams (ξ_{mis}) and wavy beams (ξ_{wvy}) can be predicted with an accuracy of over 90% (and variations in beam diameter are still predictable with an 64% accuracy), which is deemed satisfactory. This is in agreement with the correlation matrix of Figure 17, even though the latter was established for different boundary conditions (there affine homogenization, here uniaxial compression). Young's modulus is insufficient to predict node displacements. Knowledge of Poisson's ratio of either topology 1, 2, or 4, or the shear modulus of topology 4 would be required to provide the missing information on ξ_{nds}.

6.3. Predicting imperfections from experimental measurements

As a validation example, we apply the proposed machine learning framework to predict the distribution of imperfections in trusses based on experimental measurements only. To this end, we printed three samples—each one

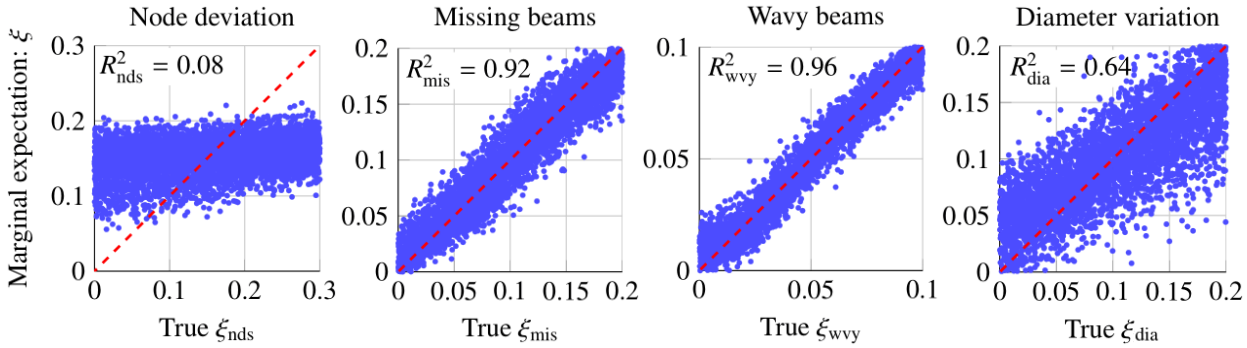

Figure 18: Accuracy of predicted marginal expectation of each imperfection vs. the true value on the test dataset, using the uniaxial Young's moduli of three 3D truss topologies (octet, bitruncated octahedron, octahedron) as input parameters. Due to the smaller number of input parameters (number of mechanical properties and number of UCs), the accuracy of the prediction decreases when compared to Figure 15. All dashed lines (in red) represent the ideal line with zero intercept and unit slope; the corresponding R^2 deviations are indicated.

of octet, bitruncated octahedron, and octahedron type. All three were designed to have identical, randomly chosen imperfections satisfying $\xi_{\text{nds}} = 0.238$, $\xi_{\text{mis}} = 0.157$, $\xi_{\text{wvy}} = 0.054$, and $\xi_{\text{dia}} = 0.113$. Figure 19 shows the three lattices before exposing them to a quasistatic compression test to identify their effective Young's moduli E^*.

The experimentally measured Young's moduli (including the correction factor of 1.2 identified in Section 5 to match differences between experiments and simulations) are $E^* = 11.8743$ MPa for the octet, $E^* = 3.0867$ MPa for the octahedron, and $E^* = 0.91776$ MPa for the bitruncated octahedron. Using these three input parameters, our machine learning framework yields the predictions in Figure 20, which captures the distributions of missing beams, wavy beams, and diameter variations well, and it even predicts node displacements (even though we discussed that this type of imperfection is hard to predict with the present framework). This confirms that our machine learning tool can predict realistic defect distributions of the chosen types from easily accessible experimental measurements.

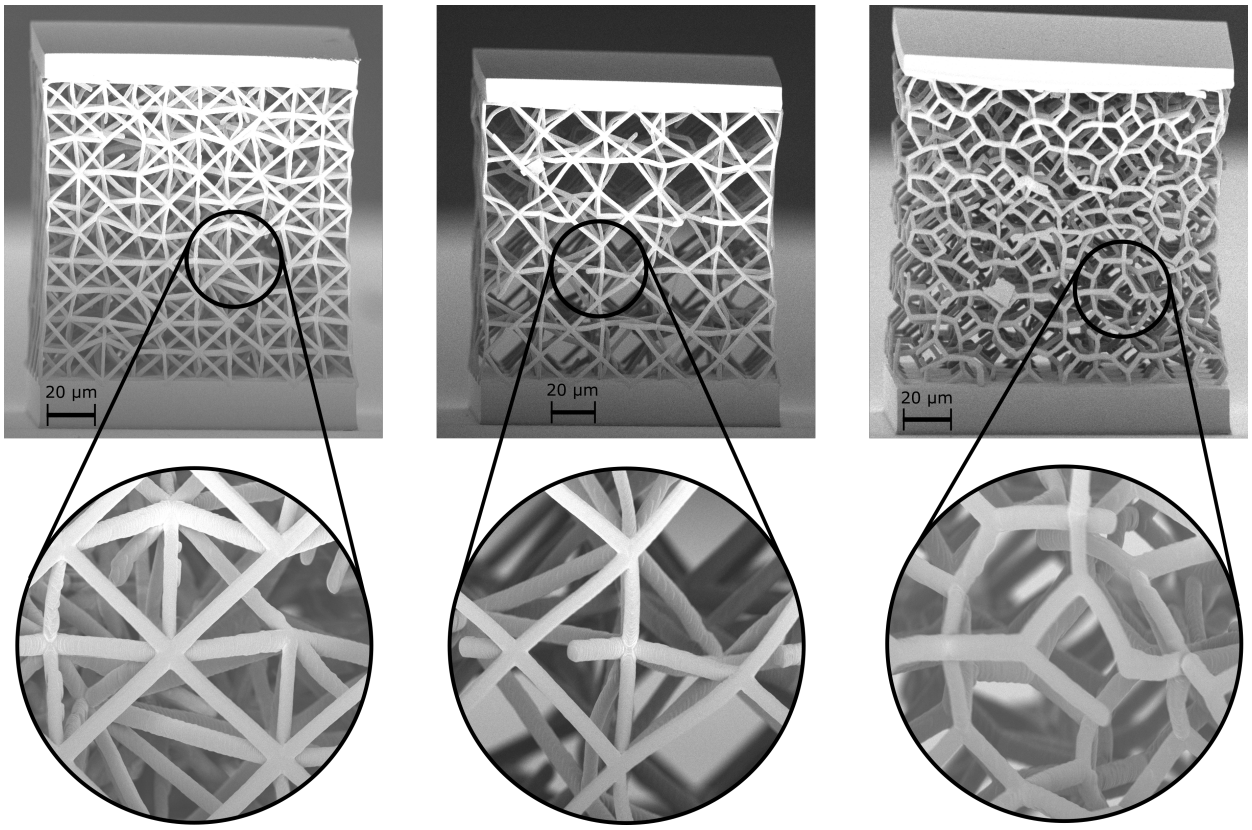

Figure 19: Fabricated octet, octahedron, and bitruncated octahedron samples (from left to right) with deliberately introduced imperfections satisfying the distributions $\xi_{\text{nds}} = 0.238$, $\xi_{\text{mis}} = 0.157$, $\xi_{\text{wvy}} = 0.054$, and $\xi_{\text{dia}} = 0.113$.

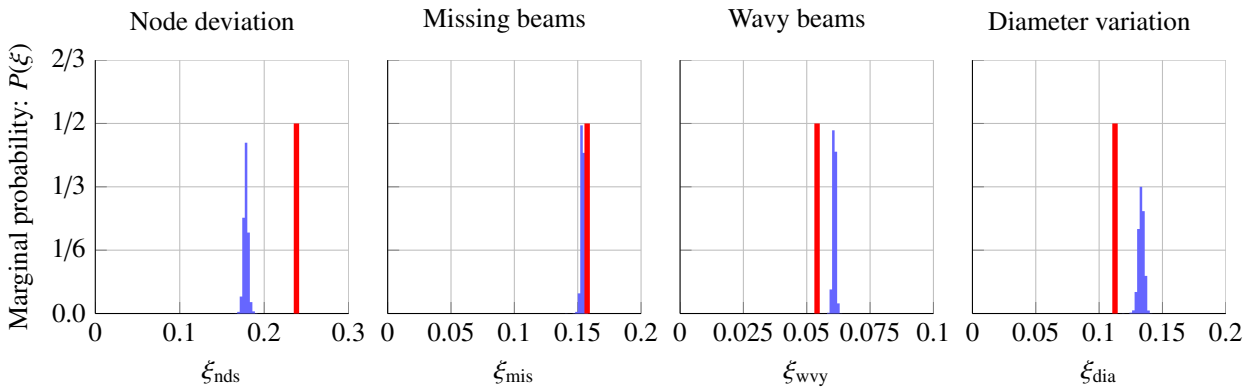

Figure 20: Predicted marginal probability distribution of imperfections based on experimental measurements on the three samples in Figure 19. The samples had the true distributions $\xi_{\text{nds}} = 0.238167$, $\xi_{\text{mis}} = 0.157455$, $\xi_{\text{wvy}} = 0.054072$, and $\xi_{\text{dia}} = 0.112529$, shown as red lines. The blue distributions are the predictions by the machine learning framework.

7. Conclusion

We have studied the sensitivity of the effective elastic properties of various 2D and 3D periodic trusses with respect to four frequently observed types of geometric imperfections. We first computed the homogenized, effective elastic properties of a total of 11 different stretching- and bending-dominated truss topologies (6 in 2D, 5 in 3D) based on affine displacements applied to large RVEs of trusses with random imperfections. (Results without imperfections matched closely with periodic homogenization.) We discussed that, while most imperfections reduce the effective stiffness, some imperfection types may even lead to stiffening of specific truss topologies. To validate the numerical framework, we further computed the uniaxial Young's modulus of 3D trusses, which was compared to experimental measurements on trusses with different types of imperfections—overall showing convincing agreement. In addition to the forward model, predicting the reduction in stiffness of defective trusses, we also presented an inverse machine learning-based approach, which predicts the defect distribution in a truss based on given elastic properties. This inverse model was trained in two flavors: first, based on the full homogenized elastic properties of five different truss topologies (which highlighted the different correlations between elastic properties and imperfection types) and, second, based on only the uniaxial stiffness of three truss topologies (which can readily be realized in experiments). Using experimentally measured Young's moduli of three trusses, their underlying defect distribution was predicted along with prediction uncertainties, overall showing convincing agreement.

The knowledge gained and the new (forward and inverse) modeling tools reported here aid to the still open challenge of incorporating fabrication-induced imperfections into the design process of truss-based architected materials. Knowledge of the property (in-)sensitivity is essential for designing structures for not only safety-relevant industrial applications. The inverse model helps identify the predominant defect types in manufactured truss architectures based on relatively simple measurements towards optimizing the design and manufacturing process [5] as well as designing structures that are less sensitive to imperfections [55].

Of course, this study can be extended in multiple directions, which also highlights its limitations. The assumption that all defect probability distributions are Gaussian and centered around the defect-free truss can be extended to, e.g., skew-normal distributions, where appropriate. Furthermore, the expectation value need not overlap with the as-designed geometry [36]. The distributions and magnitudes of the different imperfection types can also be set to those of a specific fabrication route. Going beyond elasticity, a similar strategy can be applied to study the sensitivity of the yield strength [14, 23, 50, 56] or fracture toughness [57] of trusses to imperfections.

Acknowledgments

C.M.P. and T.B. acknowledge the support from the National Science Foundation (NSF) through Career Award CMMI-2142460 and from the U.S. Army Research Office (ARO) through the MIT Institute for Soldier Nanotechnologies (ISN) under contract number W911NF-13-D-0001. R.N.G. thanks E. Courthoud for supporting the numerical implementation of the homogenization model.

References

[1] C. Chu, G. Graf, D. W. Rosen, Design for additive manufacturing of cellular structures, Computer-Aided Design and Applications 5 (5) (2008) 686–696.

[2] C. Yan, L. Hao, A. Hussein, D. Raymont, Evaluations of cellular lattice structures manufactured using selective laser melting, International Journal of Machine Tools and Manufacture 62 (2012) 32–38.

[3] B. Vayre, F. Vignat, F. Villeneuve, Metallic additive manufacturing: state-of-the-art review and prospects, Mechanics & Industry 13 (2) (2012) 89–96.

[4] M. F. Zaeh, G. Branner, Investigations on residual stresses and deformations in selective laser melting, Production Engineering 4 (1) (2010) 35–45.

[5] Z. S. Bagheri, D. Melancon, L. Liu, R. B. Johnston, D. Pasini, Compensation strategy to reduce geometry and mechanics mismatches in porous biomaterials built with selective laser melting, Journal of the mechanical behavior of biomedical materials 70 (2017) 17–27.

[6] G. Campoli, M. S. Borleffs, S. Amin Yavari, R. Wauthle, H. Weinans, A. A. Zadpoor, Mechanical properties of open-cell metallic biomaterials manufactured using additive manufacturing, Materials & Design 49 (2013) 957–965. doi:10.1016/j.matdes.2013.01.071.
URL http://www.sciencedirect.com/science/article/pii/S0261306913000940

[7] J. Grenestedt, On interactions between imperfections in cellular solids, Journal of materials science 40 (22) (2005) 5853–5857.

[8] D. Pasini, J. K. Guest, Imperfect architected materials: mechanics and topology optimization, MRS Bulletin 44 (10) (2019) 766–772.

[9] C. Coulais, A. Sabbadini, F. Vink, M. van Hecke, Multi-step self-guided pathways for shape-changing metamaterials, Nature 561 (7724) (2018) 512–515.

[10] L. R. Meza, A. J. Zelhofer, N. Clarke, A. J. Mateos, D. M. Kochmann, J. R. Greer, Resilient 3d hierarchical architected metamaterials, Proceedings of the National Academy of Sciences 112 (37) (2015) 11502–11507. arXiv:http://www.pnas.org/content/112/37/11502.full.pdf, doi:10.1073/pnas.1509120112.
URL http://www.pnas.org/content/112/37/11502.abstract

[11] X. Zheng, H. Lee, T. H. Weisgraber, M. Shusteff, J. Deotte, E. B. Duoss, J. D. Kuntz, M. M. Biener, Q. Ge, J. A. Jackson, S. O. Kucheyev, N. X. Fang, C. M. Spadaccini, Ultralight, Ultrastiff Mechanical Metamaterials, Science 344 (6190) (2014) 1373–1377.

[12] L. Meza, J. Greer, Mechanical characterization of hollow ceramic nanolattices, Journal of Materials Science 49 (6) (2014) 2496–2508.

[13] J. Bauer, A. Schroer, R. Schwaiger, O. Kraft, Approaching theoretical strength in glassy carbon nanolattices, Nature materials 15 (4) (2016) 438–443.

[14] L. Liu, P. Kamm, F. Garcia-Moreno, J. Banhart, D. Pasini, Elastic and failure response of imperfect three-dimensional metallic lattices: the role of geometric defects induced by Selective Laser Melting, Journal of the Mechanics and Physics of Solids 107 (2017) 160–184. doi:10.1016/j.jmps.2017.07.003.
URL http://www.sciencedirect.com/science/article/pii/S0022509616307608

[15] J. K. Guest, T. Igusa, Structural optimization under uncertain loads and nodal locations, Computer Methods in Applied Mechanics and Engineering 198 (1) (2008) 116–124.

[16] D. Melancon, Z. Bagheri, R. Johnston, L. Liu, M. Tanzer, D. Pasini, Mechanical characterization of structurally porous biomaterials built via additive manufacturing: experiments, predictive models, and design maps for load-bearing bone replacement implants, Acta biomaterialia 63 (2017) 350–368.

[17] D. D. Symons, N. A. Fleck, The Imperfection Sensitivity of Isotropic Two-Dimensional Elastic Lattices, Journal of Applied Mechanics 75 (5) (2008) 051011. doi:10.1115/1.2913044.
URL https://appliedmechanics.asmedigitalcollection.asme.org/article.aspx?articleid=1418997

[18] X. Liu, N. Liang, Effective elastic moduli of triangular lattice material with defects, Journal of the Mechanics and Physics of Solids 60 (10) (2012) 1722–1739. doi:10.1016/j.jmps.2012.06.006.
URL http://www.sciencedirect.com/science/article/pii/S0022509612001263

[19] X.-D. E. Guo, T. A. McMahon, T. M. Keaveny, W. C. Hayes, L. J. Gibson, Finite element modeling of damage accumulation in trabecular bone

under cyclic loading, Journal of Biomechanics 27 (2) (1994) 145 – 155. doi:https://doi.org/10.1016/0021-9290(94)90203-8.
URL http://www.sciencedirect.com/science/article/pii/0021929094902038

[20] X. Guo, L. J. Gibson, Behavior of intact and damaged honeycombs: a finite element study, International Journal of Mechanical Sciences 41 (1) (1999) 85 – 105. doi:https://doi.org/10.1016/S0020-7403(98)00037-X.
URL http://www.sciencedirect.com/science/article/pii/S002074039800037X

[21] M. J. Silva, L. J. Gibson, The effects of non-periodic microstructure and defects on the compressive strength of two-dimensional cellular solids, International Journal of Mechanical Sciences 39 (5) (1997) 549–563.

[22] K. Li, X. L. Gao, G. Subhash, Effects of cell shape and cell wall thickness variations on the elastic properties of two-dimensional cellular solids, International Journal of Solids and Structures 42 (5) (2005) 1777–1795. doi:10.1016/j.ijsolstr.2004.08.005.
URL http://www.sciencedirect.com/science/article/pii/S0020768304004536

[23] C. Chen, T. Lu, N. Fleck, Effect of imperfections on the yielding of two-dimensional foams, Journal of the Mechanics and Physics of Solids 47 (11) (1999) 2235–2272.

[24] A. Gross, P. Pantidis, K. Bertoldi, S. Gerasimidis, Correlation between topology and elastic properties of imperfect truss-lattice materials, Journal of the Mechanics and Physics of Solids 124 (2019) 577–598. doi:10.1016/j.jmps.2018.11.007.
URL http://www.sciencedirect.com/science/article/pii/S0022509618308615

[25] D. Queheillalt, V. Deshpande, H. Wadley, Truss waviness effects in cellular lattice structures, Journal of Mechanics of Materials and Structures 2 (9) (2007) 1657–1675.

[26] R. Rinaldi, J. Bernal-Ostos, C. Hammetter, A. Jacobsen, F. Zok, Effects of material heterogeneities on the compressive response of thiol-ene pyramidal lattices, Journal of Materials Science 47 (18) (2012) 6621–6632.

[27] J. Wallach, L. Gibson, Defect sensitivity of a 3d truss material, Scripta Materialia 45 (6) (2001) 639 – 644. doi:https://doi.org/10.1016/S1359-6462(01)01073-9.
URL http://www.sciencedirect.com/science/article/pii/S1359646201010739

[28] R. M. Latture, M. R. Begley, F. W. Zok, Defect sensitivity of truss strength, Journal of the Mechanics and Physics of Solids 124 (2019) 489–504.

[29] T. Tancogne-Dejean, A. B. Spierings, D. Mohr, Additively-manufactured metallic micro-lattice materials for high specific energy absorption under static and dynamic loading, Acta Materialia 116 (2016) 14–28.

[30] L. Xiao, W. Song, C. Wang, H. Liu, H. Tang, J. Wang, Mechanical behavior of open-cell rhombic dodecahedron ti–6al–4v lattice structure, Materials Science and Engineering: A 640 (2015) 375–384.

[31] A. Vigliotti, V. S. Deshpande, D. Pasini, Non linear constitutive models for lattice materials, Journal of the Mechanics and Physics of Solids 64 (2014) 44 – 60. doi:https://doi.org/10.1016/j.jmps.2013.10.015.
URL http://www.sciencedirect.com/science/article/pii/S0022509613002238

[32] V. S. Deshpande, N. A. Fleck, M. F. Ashby, Effective properties of the octet-truss lattice material, Journal of the Mechanics and Physics of Solids 49 (8) (2001) 1747–1769. doi:10.1016/S0022-5096(01)00010-2.
URL http://www.sciencedirect.com/science/article/pii/S0022509601000102

[33] R. N. Glaesener, C. Lestringant, B. Telgen, D. M. Kochmann, Continuum models for stretching- and bending-dominated periodic trusses undergoing finite deformations, International Journal of Solids and Structures 171 (2019) 117–134. doi:10.1016/j.ijsolstr.2019.04.022.
URL http://www.sciencedirect.com/science/article/pii/S002076831930191X

[34] R. N. Glaesener, E. A. Träff, B. Telgen, R. M. Canonica, D. M. Kochmann, Continuum representation of nonlinear three-dimensional periodic truss networks by on-the-fly homogenization, International Journal of Solids and Structures 206 (2020) 101 – 113. doi:https://doi.org/10.1016/j.ijsolstr.2020.08.013.
URL http://www.sciencedirect.com/science/article/pii/S0020768320303127

[35] R. N. Glaesener, J.-H. Bastek, F. Gonon, V. Kannan, B. Telgen, B. Spöttling, S. Steiner, D. M. Kochmann, Viscoelastic truss metamaterials

as time-dependent generalized continua, Journal of the Mechanics and Physics of Solids 156 (2021) 104569. doi:https://doi.org/10.1016/j.jmps.2021.104569.
URL https://www.sciencedirect.com/science/article/pii/S0022509621002180

[36] A. El Elmi, D. Melancon, M. Asgari, L. Liu, D. Pasini, Experimental and numerical investigation of selective laser melting–induced defects in ti–6al–4v octet truss lattice material: the role of material microstructure and morphological variations, Journal of Materials Research 35 (15) (2020) 1900–1912.

[37] L. J. Gibson, Biomechanics of cellular solids, Journal of Biomechanics 38 (3) (2005) 377–399. doi:10.1016/j.jbiomech.2004.09.027.
URL http://www.sciencedirect.com/science/article/pii/S0021929004004919

[38] G. E. P. Box, M. E. Muller, A note on the generation of random normal deviates, Ann. Math. Statist. 29 (2) (1958) 610–611. doi:10.1214/aoms/1177706645.
URL https://doi.org/10.1214/aoms/1177706645

[39] S. Arabnejad, R. B. Johnston, J. A. Pura, B. Singh, M. Tanzer, D. Pasini, High-strength porous biomaterials for bone replacement: A strategy to assess the interplay between cell morphology, mechanical properties, bone ingrowth and manufacturing constraints, Acta biomaterialia 30 (2016) 345–356.

[40] J. Bauer, L. R. Meza, T. A. Schaedler, R. Schwaiger, X. Zheng, L. Valdevit, Nanolattices: An Emerging Class of Mechanical Metamaterials, Advanced Materials 29 (40) (2017) 1701850. doi:10.1002/adma.201701850.
URL https://onlinelibrary.wiley.com/doi/full/10.1002/adma.201701850

[41] G. P. Steven, Homogenization of multicomponent composite orthotropic materials using fea, Communications in numerical methods in engineering 13 (7) (1997) 517–531.

[42] T. Kanit, S. Forest, I. Galliet, V. Mounoury, D. Jeulin, Determination of the size of the representative volume element for random composites: statistical and numerical approach, International Journal of solids and structures 40 (13-14) (2003) 3647–3679.

[43] M. Ostoja-Starzewski, Material spatial randomness: From statistical to representative volume element, Probabilistic engineering mechanics 21 (2) (2006) 112–132.

[44] C. Miehe, A. Koch, Computational micro-to-macro transitions of discretized microstructures undergoing small strains, Archive of Applied Mechanics 72 (4) (2002) 300–317. doi:10.1007/s00419-002-0212-2.
URL https://doi.org/10.1007/s00419-002-0212-2

[45] W. Voigt, Lehrbuch der kristallphysik:(mit ausschluss der kristalloptik), Vol. 34, BG Teubner, 1910.

[46] V. Deshpande, M. Ashby, N. Fleck, Foam topology: bending versus stretching dominated architectures, Acta Materialia 49 (6) (2001) 1035 – 1040. doi:https://doi.org/10.1016/S1359-6454(00)00379-7.
URL http://www.sciencedirect.com/science/article/pii/S1359645400003797

[47] B. Telgen, O. Sigmund, D. M. Kochmann, Topology optimization of graded truss lattices based on on-the-fly homogenization, Journal of Applied Mechanics 89 (6) (2022) 061006.

[48] J. Peters, M. Muthuswamy, J. Wibowo, A. Tordesillas, Characterization of force chains in granular material, Physical review E 72 (4) (2005) 041307.

[49] C. Chen, T. Lu, N. Fleck, Effect of inclusions and holes on the stiffness and strength of honeycombs, International Journal of Mechanical Sciences 43 (2) (2001) 487–504.

[50] A. Simone, L. Gibson, The effects of cell face curvature and corrugations on the stiffness and strength of metallic foams, Acta Materialia 46 (11) (1998) 3929–3935.

[51] L. R. Meza, G. P. Phlipot, C. M. Portela, A. Maggi, L. C. Montemayor, A. Comella, D. M. Kochmann, J. R. Greer, Reexamining the mechanical property space of three-dimensional lattice architectures, Acta Materialia 140 (2017) 424 – 432. doi:https://doi.org/10.1016/j.actamat.2017.08.052.
URL http://www.sciencedirect.com/science/article/pii/S1359645417307073

[52] C. M. Portela, J. R. Greer, D. M. Kochmann, Impact of node geometry on the effective stiffness of non-slender three-dimensional truss lattice

architectures, Extreme Mechanics Letters 22 (2018) 138 – 148. doi:https://doi.org/10.1016/j.eml.2018.06.004.
URL http://www.sciencedirect.com/science/article/pii/S2352431618300725

[53] C. M. Portela, J. R. Greer, D. M. Kochmann, Impact of node geometry on the effective stiffness of non-slender three-dimensional truss lattice architectures, Extreme Mechanics Letters 22 (2018) 138–148.

[54] M. Dallago, S. Raghavendra, V. Luchin, G. Zappini, D. Pasini, M. Benedetti, The role of node fillet, unit-cell size and strut orientation on the fatigue strength of ti-6al-4v lattice materials additively manufactured via laser powder bed fusion, International Journal of Fatigue 142 (2021) 105946.

[55] A. Moussa, D. Melancon, A. El Elmi, D. Pasini, Topology optimization of imperfect lattice materials built with process-induced defects via powder bed fusion, Additive Manufacturing 37 (2021) 101608.

[56] N. A. Fleck, X. Qiu, The damage tolerance of elastic–brittle, two-dimensional isotropic lattices, Journal of the Mechanics and Physics of Solids 55 (3) (2007) 562 – 588. doi:https://doi.org/10.1016/j.jmps.2006.08.004.
URL http://www.sciencedirect.com/science/article/pii/S0022509606001359

[57] N. E. Romijn, N. A. Fleck, The fracture toughness of planar lattices: Imperfection sensitivity, Journal of the Mechanics and Physics of Solids 55 (12) (2007) 2538–2564.

[58] D. P. Kingma, M. Welling, Auto-encoding variational bayes (2013). doi:10.48550/ARXIV.1312.6114.
URL https://arxiv.org/abs/1312.6114

[59] K. Sohn, H. Lee, X. Yan, Learning structured output representation using deep conditional generative models, in: C. Cortes, N. Lawrence, D. Lee, M. Sugiyama, R. Garnett (Eds.), Advances in Neural Information Processing Systems, Vol. 28, Curran Associates, Inc., 2015.
URL https://proceedings.neurips.cc/paper/2015/file/8d55a249e6baa5c06772297520da2051-Paper.pdf

[60] S. Kullback, R. A. Leibler, On information and sufficiency, The Annals of Mathematical Statistics 22 (1) (1951) 79–86. doi:10.1214/aoms/1177729694.
URL https://doi.org/10.1214/aoms/1177729694

[61] D. P. Kingma, J. Ba, Adam: A method for stochastic optimization (2014). doi:10.48550/ARXIV.1412.6980.
URL https://arxiv.org/abs/1412.6980

[62] A. Paszke, S. Gross, F. Massa, A. Lerer, J. Bradbury, G. Chanan, T. Killeen, Z. Lin, N. Gimelshein, L. Antiga, A. Desmaison, A. Köpf, E. Yang, Z. DeVito, M. Raison, A. Tejani, S. Chilamkurthy, B. Steiner, L. Fang, J. Bai, S. Chintala, Pytorch: An imperative style, high-performance deep learning library (2019). doi:10.48550/ARXIV.1912.01703.
URL https://arxiv.org/abs/1912.01703

Appendix A. Periodic vs. affine boundary conditions for homogenization

We compute the effective response of trusses with random imperfections by applying affine displacement boundary conditions to large RVEs (containing the numbers of UCs reported in Tables 3 and 4). Periodic boundary conditions are unfortunately problematic in this setting. As affine displacement boundary conditions generally over-predict the effective stiffness, we here compare the computed homogenized properties of defect-free trusses using both periodic homogenization [33, 34] and the here chosen affine displacement assumption.

Table A.1 compares the effective Young's modulus $\bar{E}$, effective Poisson's ratio $\bar{\nu}$, and the effective shear modulus $\bar{G}$, all calculated from a single RUC with periodic BCs [33] as well as from the RVEs in Tables 3 and 4 with affine displacement boundary conditions. Results show a good agreement between the effective properties, confirming the appropriateness of the chosen affine displacement approach. Only for strongly bending-dominated topologies such as the hexagon and diamond topologies in 2D as well as for the bitruncated octahedron and the diamond in 3D, the

	Periodic BCs			Affine displacement BCs		
2D	$\overline{E}/E$	$\overline{\nu}$	$\overline{G}/E$	$\overline{E}/E$	$\overline{\nu}$	$\overline{G}/E$
Cross	$1.127 \cdot 10^{-2}$	0.405	$5.583 \cdot 10^{-3}$	$1.127 \cdot 10^{-2}$	0.405	$5.583 \cdot 10^{-3}$
Triangle	$9.114 \cdot 10^{-3}$	0.330	$3.434 \cdot 10^{-3}$	$9.194 \cdot 10^{-3}$	0.330	$3.426 \cdot 10^{-3}$
Hexagon	$6.652 \cdot 10^{-5}$	0.971	$1.688 \cdot 10^{-5}$	$7.613 \cdot 10^{-3}$	0.961	$1.689 \cdot 10^{-5}$
Square	$7.854 \cdot 10^{-3}$	0.0	$2.945 \cdot 10^{-5}$	$7.854 \cdot 10^{-5}$	0.0	$2.945 \cdot 10^{-5}$
Diamond	$8.268 \cdot 10^{-5}$	0.985	$2.777 \cdot 10^{-3}$	$8.807 \cdot 10^{-5}$	0.984	$2.777 \cdot 10^{-3}$
Kagome	$2.274 \cdot 10^{-3}$	0.331	$8.536 \cdot 10^{-4}$	$2,274 \cdot 10^{-3}$	0.331	$8.534 \cdot 10^{-4}$
3D	$\overline{E}/E$	$\overline{\nu}$	$\overline{G}/E$	$\overline{E}/E$	$\overline{\nu}$	$\overline{G}/E$
Octet	$7.553 \cdot 10^{-3}$	0.33	$5.595 \cdot 10^{-3}$	$7.554 \cdot 10^{-3}$	0.33	$5.595 \cdot 10^{-3}$
Octahedron	$3.776 \cdot 10^{-3}$	0.33	$2.790 \cdot 10^{-3}$	$3.777 \cdot 10^{-3}$	0.33	$2.790 \cdot 10^{-3}$
Bitr. Oct.	$4.134 \cdot 10^{-5}$	0.493	$1.363 \cdot 10^{-5}$	$5.445 \cdot 10^{-5}$	0.490	$2.240 \cdot 10^{-5}$
Cube	$7.854 \cdot 10^{-3}$	0.0	$2.945 \cdot 10^{-5}$	$7.863 \cdot 10^{-3}$	0.0	$2.947 \cdot 10^{-5}$
Diamond	$3.812 \cdot 10^{-5}$	0.494	$3.769 \cdot 10^{-5}$	$3.773 \cdot 10^{-5}$	0.494	$3.660 \cdot 10^{-5}$

Table A.1: Comparison of the effective elastic properties of different 2D and 3D truss topologies as obtained from homogenization with periodic boundary conditions (using an in-house code and formulation [33]) vs. affine displacement boundary conditions. Moduli are normalized by the base material's Young's modulus E. Poisson's ratio of the base material is $\nu = 0.49$. All beams have a slenderness ratio of $\lambda = 0.1$, except for the cross topology in 2D, which has two sets of beams with different lengths, where the shorter beams have a slenderness ratio of $\lambda = 0.14$.

deviations between the two approaches is appreciable.

Appendix B. Choice of RVE and ensemble sizes

Imposing random imperfections onto a perfect lattice results in an infinite range of imperfect structures. A statistically appropriate computation of the effective properties requires a sufficiently large RVE. Since an ideal, infinite RVE size is computationally untractable, we choose a finite-size RVE, which must be sufficiently large (*spatial averaging criterion*). In addition, we compute the effective response by averaging over a ensemble of N different random realizations, which must be sufficiently large (*ensemble averaging criterion*) as well. For practical reasons, we choose the RVE size sufficiently small to allow for efficient computations and to fit within a 3D quadrilateral (2D quadratic) domain. For an RVE much larger than the size of the UC and of the imperfections and for large N, the average stiffness $\tilde{\mathbb{C}}(N) = \frac{1}{N}\sum_{i=1}^{N}\tilde{\mathbb{C}}_i$ converges to it the true effective stiffness $\mu = \mathbb{C}^*$ as a Gaussian distribution by the central limit theorem. We compute the confidence interval $\left(\mu - z^*\frac{\sigma}{\sqrt{N}}, \mu + z^*\frac{\sigma}{\sqrt{N}}\right)$ and the resulting effective variance (margin of error) $e = z^*\frac{\sigma}{\sqrt{N}}$. We select the critical value $z^* = 1.96$ within a z-statistic for a confidence level of 95%; μ is the ensemble mean stiffness, σ describes the standard deviation (visualized in the shape of error bars in all examples). The selected RVE sizes presented in Tables 3 and 4, combined with a total number of $N = 100$ random samples, guarantees for almost all geometries and imperfection types a margin of error $e < 0.1\%$. Therefore, we deem the chosen RVE and ensemble sizes sufficient. Exceptions are the Poisson's ratio sensitivity towards node displacements and missing beams of the kagome structure, where the margins of error increase to $e = 0.37\%$ and $e = 0.79\%$, respectively (see the standard deviation in Figure 5f). We attribute this large standard deviation to the relatively small $\bar{\mathbb{C}}_{1122}$ stiffness tensor component of the kagome lattice (Table A.1), when compared to the other components.

Figure B.21 visualizes the convergence of the effective Young's modulus $\bar{E}$ for the example of the bitruncated octahedron. On the left, we show for the example of missing beams at $\xi_{\text{mis}} = 0.2$ how $\bar{E}$ converges with increasing

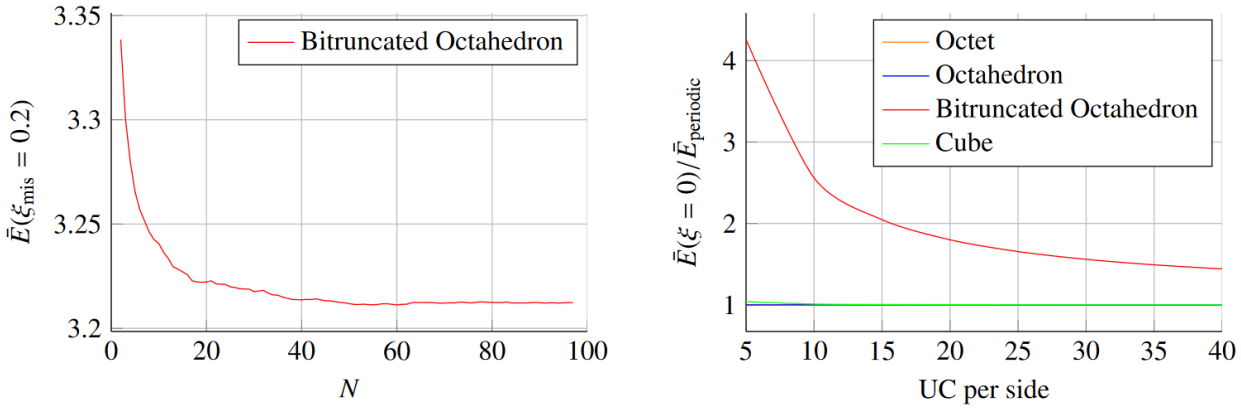

Figure B.21: On the left, the effect of ensemble averaging is visualized for the example of a bitruncated octahedron lattice with $\xi_{\text{mis}} = 0.2$. On the right, the spatial averaging criterion shows how, with increasing mesh refinement, the effective response converges to the one evaluated using the continuum model described in Section Appendix A

ensemble size, using an RVE size of 40×40×40 UC. On the right, the convergence of $\bar{E}$ is shown with increasing RVE size (each data point is computed from $N = 100$ realizations). In case of the bitruncated octahedron an even larger mesh size would be required to improve the result; however, running several simulations with an assembly larger than $40 \times 40 \times 40$ becomes computationally infeasible.

Appendix C. Comparison to existing literature

As explained in the introduction, prior studies have numerically probed the sensitivity of different truss topologies to imperfections. For reference, we here compare our results in Figures 5 and 6 to findings in literature. While we selected a constant slenderness ratio of $\lambda = 0.1$ in all our simulations in Figures 5 and 6, we here change this value for a comparison with literature data. Symons and Fleck [17] used a slenderness ratio of $\lambda = 0.02$ for their study of missing beams in triangular, hexagonal, and kagome lattices. Recently, Liu and Liang [18] studied triangular lattices with $\lambda = 0.043$, while Gross et al. [24] used $\lambda = 0.05$ in their 3D simulations. For the purpose of a comparison, we reran the simulations for missing beams for a selection of 2D and 3D topologies, to allow for a comparison of our approach with those stated above. In 2D, Figure C.22 shows good agreement with the results in [18] (who used periodic BCs and beam elements) to compute the effective mechanical properties for the triangular lattice when subjected to missing beams. The result for the bulk modulus $\bar{G}$ also agrees with observations in [17]. These authors further studied the sensitivity of $\bar{G}$ to the number of missing beams for the hexagonal and kagome lattices, which also agree with our data. The comparison to studies that select different slenderness ratios sheds light on this additional parameter, which also has a determining influence on the sensitivity. While the $\bar{G}$-sensitivity for the hexagonal (red) and triangular (blue) topologies remains almost unchanged when decreasing the slenderness ratio from $\lambda = 0.1$ to $\lambda = 0.02$, the shear-stiffness of the kagome lattice drops faster for slender beams, when compared to our results from Figure 5.

In 3D, the study by Gross et al. [24] on the sensitivity of different topologies to an increasing amount of missing beams, using periodic BCs and the finite element method with Timoshenko beams, permits a direct comparison with our results (see Figure C.23). Compared to our data, their study shows almost identical results for Young's modulus and the shear modulus for the octet and octahedral topologies (marked in orange and blue, respectively) but a different sensitivity to missing beams in case of the bitruncated octahedron. Interestingly, our numerical data for the shear modulus of the bitruncated octahedron agree excellently with the *analytical* predictions from the literature [24] up to $\xi_{\text{mis}} \leq 0.15$, unlike the *numerical* data reported within the same publication [24]. We cannot conclusive explain the differences in the numerically obtained data for the bitruncated octahedron but our agreement with the analytical solution makes us confident that the data reported here are trustworthy.

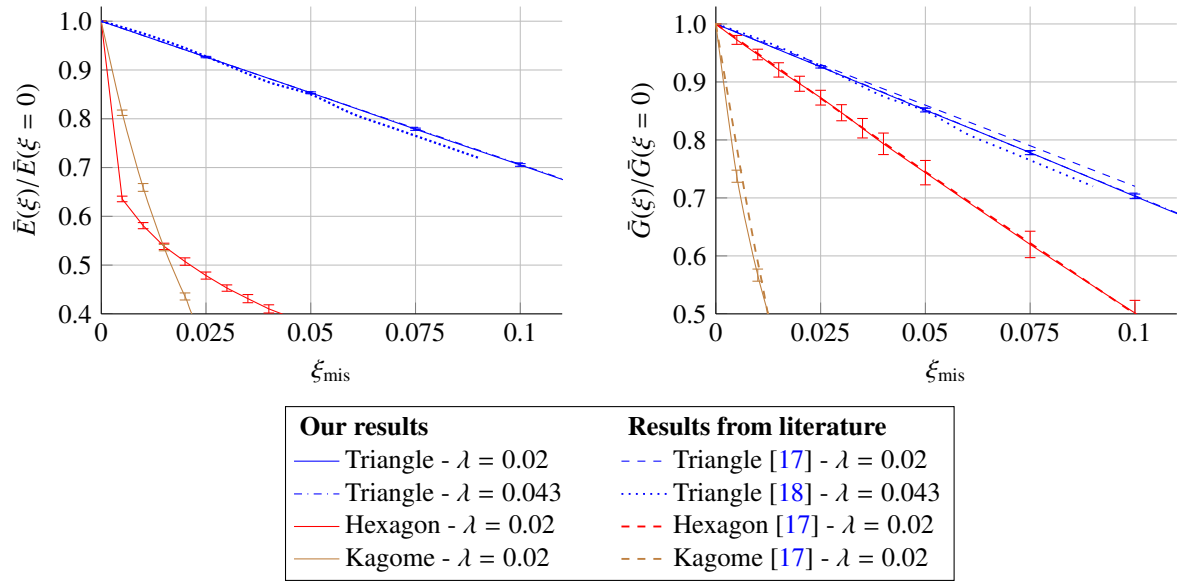

Figure C.22: Comparison of the sensitivity of Young's modulus and the shear modulus to missing beams with increasing ξ_{mis} for selected **2D** truss topologies to literature results [14, 17]. The sensitivity of the triangular lattice for slenderness ratios of $\lambda = 0.02$ and $\lambda = 0.043$ is almost identical.

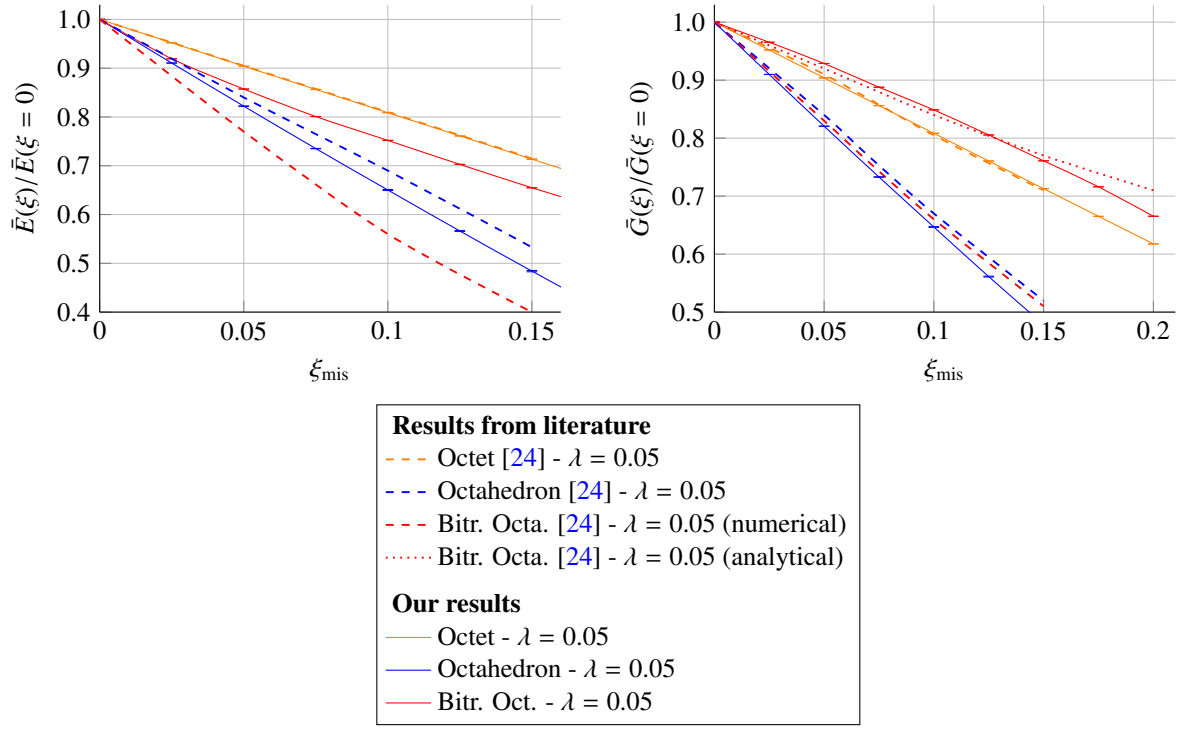

Figure C.23: Comparison of the sensitivity of the Young and shear moduli to missing beams with increasing ξ_{mis} for selected **3D** truss topologies to results in [24] for randomly removed beams.

Appendix D. Machine learning framework for predicting imperfections based on deviations in mechanical properties

We use a conditional variational autoencoder (CVAE) [58, 59] to predict probabilistic estimates of the imperfections, i.e., probability $P(\boldsymbol{\xi})$ based on a set of given imperfect mechanical properties, $\boldsymbol{\chi}$. Figure 14 schematically illustrates the CVAE framework, which consists of a feed-forward neural network called the *encoder*, a probabilistic *latent space*, and another feed-forward neural network called the *decoder*. In the following, we describe each component of the framework.

Encoder: For a given pair of $\boldsymbol{\xi}$ and $\boldsymbol{\chi}$ from the training dataset, the encoder receives as input their concatenation, i.e., $(\boldsymbol{\xi},\boldsymbol{\chi}) \in \mathbb{R}^{\dim(\boldsymbol{\xi})+\dim(\boldsymbol{\chi})}$. The encoder outputs two vectors: $\boldsymbol{\mu} \in \mathbb{R}^d$ and $\boldsymbol{s} \in \mathbb{R}^d$, where d is treated as a hyperparameter. The interpretation of $\boldsymbol{\mu}$ and $\boldsymbol{s}$ as well as d are discussed later. For the scope of this work, we model the encoder architecture as

$$\begin{aligned} \boldsymbol{\mu} &= \mathcal{L}_{\omega_2}^{h\to d} \circ \mathcal{R} \circ \mathcal{L}_{\omega_1}^{\dim(\boldsymbol{\xi})+\dim(\boldsymbol{\chi})\to h}[(\boldsymbol{\xi},\boldsymbol{\chi})], \\ \boldsymbol{s} &= \mathcal{L}_{\omega_3}^{h\to d} \circ \mathcal{R} \circ \mathcal{L}_{\omega_1}^{\dim(\boldsymbol{\xi})+\dim(\boldsymbol{\chi})\to h}[(\boldsymbol{\xi},\boldsymbol{\chi})]. \end{aligned} \tag{D.1}$$

Here, $\mathcal{L}_{\omega_k}^{i\to j}$ denotes a linear layer parameterized by the set of trainable weights and biases $\omega_k = \{\boldsymbol{A}_k, \boldsymbol{b}_k\}$ such that any $\boldsymbol{v} \in \mathbb{R}^i$ is transformed according to

$$\mathcal{L}_{\omega_k}^{i\to j}[\boldsymbol{v}] = \boldsymbol{A}_k\boldsymbol{v} + \boldsymbol{b}_k, \qquad \text{with} \quad \boldsymbol{A}_k \in \mathbb{R}^{j\times i}, \boldsymbol{b}_k \in \mathbb{R}^j. \tag{D.2}$$

Similar to the output dimension d, the hidden/intermediate dimension h is treated as a hyperparameter. $\mathcal{R}(\cdot) = \max(0,\cdot)$ is the rectified linear activation unit (ReLU), which acts element-wise on the input and introduces nonlinearity to the series of linear transformations. All the trainable parameters of the encoder are collectively denoted as $\omega_E = \{\omega_1, \omega_2, \omega_3\}$.

Latent space: During the training phase of the CVAE, the outputs of the encoder, i.e., $\boldsymbol{\mu}$ and $\boldsymbol{s}$, are interpreted as mean and log-variance of a Gaussian distribution, respectively. We sample a *latent space representation* $\boldsymbol{z} \in \mathbb{R}^d$ of the encoder inputs $(\boldsymbol{\xi},\boldsymbol{\chi})$ as

$$\boldsymbol{z} \sim \mathcal{N}\left([\mu_1,\ldots,\mu_d]^\intercal, \operatorname{diag}\left(\left[\sigma_1^2,\ldots,\sigma_d^2\right]^\intercal\right)\right), \tag{D.3}$$

where $s_i = \log(\sigma_i^2)$ is the log-variance (alternatively, $\sigma_i = \exp(s_i/2)$ is the standard deviation) of the i^{th} component. $\operatorname{diag}(\cdot)$ denotes the diagonal matrix created using the input vector $(\cdot)$, and $\mathcal{N}$ denotes the Gaussian distribution. From an implementation perspective, $\boldsymbol{z}$ is sampled as

$$\boldsymbol{z} = \boldsymbol{\mu} + \boldsymbol{\varepsilon} \odot [\sigma_1,\ldots,\sigma_d]^\intercal \qquad \text{with} \quad \boldsymbol{\varepsilon} \sim \mathcal{N}(\boldsymbol{0}, \boldsymbol{I}), \tag{D.4}$$

where $\odot$ denotes element-wise multiplication. Also known as the reparameterization trick [58], (D.4) is specifically used to sample the distribution while maintaining the differentiability required for back-propagation-based training of the neural networks.

Decoder: The latent space representation z and the imperfect mechanical properties $\boldsymbol{\chi}$ are concatenated and passed as input to the decoder. Based on those, it predicts the imperfection characteristics $\hat{\boldsymbol{\xi}} \in \mathbb{R}^{\dim(\boldsymbol{\xi})}$. Similar to the encoder, we model the decoder architecture as

$$\hat{\boldsymbol{\xi}} = \mathcal{L}_{\omega_5}^{h\to\dim(\boldsymbol{\xi})} \circ \mathcal{R} \circ \mathcal{L}_{\omega_4}^{d+\dim(\boldsymbol{\chi})\to h}[(z,\boldsymbol{\chi})] \tag{D.5}$$

with $\omega_D = \{\omega_4, \omega_5\}$ containing the trainable parameters of the decoder.

Training: Given a representative dataset $\mathcal{D} = \{(\boldsymbol{\xi}^{(n)}, \boldsymbol{\chi}^{(n)}) : n = 1, \dots, N\}$, the encoder and decoder training (i.e., finding appropriate trainable parameters ω_E and ω_D, respectively) is formulated as a minimization problem of the form:

$$\min_{\omega_E,\, \omega_D} \underbrace{\frac{1}{N}\sum_{n=1}^{N} \left\|\boldsymbol{\xi}^{(n)} - \hat{\boldsymbol{\xi}}^{(n)}\right\|^2}_{\text{reconstruction loss}} + \underbrace{\sum_{n=1}^{N} \mathrm{D}_{\mathrm{KL}}\Big(\mathcal{N}\left([\mu_1^{(n)}, \dots, \mu_d^{(n)}]^\intercal, \operatorname{diag}\left(\left[\sigma_1^{(n)2}, \dots, \sigma_d^{(n)2}\right]^\intercal\right)\right) \,\|\, \mathcal{N}(\mathbf{0}, \mathbf{I})\Big)}_{\text{Kullback–Leibler divergence loss}}. \tag{D.6}$$

The *reconstruction loss* ensures that the input to the encoder $\boldsymbol{\xi}^{(n)}$ (i.e., the imperfection characteristics) – conditioned upon a given set of mechanical properties $\boldsymbol{\chi}^{(n)}$ – is accurately reconstructed by the decoder into $\hat{\boldsymbol{\xi}}^{(n)}$. Due to the probabilistic informational bottleneck between the encoder and decoder, an accurate reconstruction of the dataset may be interpreted as learning a compressed and continuous latent representation z of input $\boldsymbol{\xi}^{(n)}$ conditioned upon $\boldsymbol{\chi}^{(n)}$. The *Kullback–Leibler divergence (KLD)* loss in (D.6) penalizes the divergence of the latent space distribution (see (D.3)) from the standard Gaussian distribution. As discussed later, ensuring that the latent space can be approximated by a standard Gaussian distribution is critical to solve the inverse problem of estimating $\boldsymbol{\xi}$ based only on known $\boldsymbol{\chi}$. The KLD between two probability distributions P and Q is given by [60]

$$\mathrm{D}_{\mathrm{KL}}(P \,\|\, Q) = \int_{-\infty}^{\infty} p(\boldsymbol{x}) \log\left(\frac{p(\boldsymbol{x})}{q(\boldsymbol{x})}\right) \mathrm{d}\boldsymbol{x}, \tag{D.7}$$

where p and q denote the probability densities of P and Q, respectively. For the case of Gaussian distributions, the KLD loss in (D.6) simplifies to

$$\mathrm{D}_{\mathrm{KL}}\Big(\mathcal{N}\left([\mu_1, \dots, \mu_d]^\intercal, \operatorname{diag}\left(\left[\sigma_1^2, \dots, \sigma_d^2\right]^\intercal\right)\right) \,\|\, \mathcal{N}(\mathbf{0}, \boldsymbol{I})\Big) \;=\; \frac{1}{2}\sum_{i=1}^{d}\left(\sigma_i^2 + \mu_i^2 - 1 - \log(\sigma_i^2)\right), \tag{D.8}$$

where the superscripts $(\cdot)^{(n)}$ have been omitted for better readability.

Inference: During the inference phase, the imperfections $\boldsymbol{\xi}$ are the unknowns to be estimated given the mechanical properties $\boldsymbol{\chi}$. Assuming that the model is trained sufficiently such that the latent space distribution can be approximated by the standard Gaussian distribution (ensured by minimizing the KLD loss in (D.6)), the latent vector z is sampled as

$$z \sim \mathcal{N}(\mathbf{0}, \boldsymbol{I}) \tag{D.9}$$

(instead of using the encoder) and concatenated with the known $\boldsymbol{\chi}$. The encoder is ignored during the inference phase. The concatenated vector $(z, \boldsymbol{\chi})$ is mapped by the decoder to $\hat{\boldsymbol{\xi}}$. The inference process can be repeated M times by sampling z via (D.9) to empirically obtain $P(\boldsymbol{\xi})$.

Implementation details: To ensure faster training and high prediction accuracy, all data features in $\mathcal{D}$ are independently and linearly scaled to the range of $[-1, 1]$ before training. Note that the results during the inference phase are scaled back to their original range after prediction from the decoder. Across all the results presented here, we use $d = 6$ as the latent space dimension and $h = 128$ as the hidden dimension in the encoder and decoder architectures. For training, we minimize the loss in (D.6) with the *Adam* optimizer [61] for 2000 epochs with a learning rate of 10^{-4} and batch size of 1024. For inference, we sample $M = 3000$ predictions to obtain representative probability distributions. All implementations are performed in PyTorch [62].